Long term effect of operating loads on large monopile-supported offshore wind turbines in sand

Aliyu Abdullahi [a,c], Subhamoy Bhattacharya [a], Chao Li [b], Yiqing Xiao [b], Ying Wang [a,b,*]

[a] Department of Civil and Environmental Engineering, University of Surrey, UK
[b] School of Civil and Environmental Engineering, Harbin Institute of Technology, Shenzhen, China
[c] Department of Civil Engineering, Federal University of Technology, Minna, Nigeria

ARTICLE INFO

ABSTRACT

Offshore wind turbines (OWTs) are known to experience modal property and foundation tilt changes during operation. These may negatively influence their serviceability and can lead to failure. To avoid these, a comprehensive characterisation of the behavioural patterns of OWTs, especially emergent large ones supported on monopiles, is necessary. In this study, environmental data collected from the proposed prototype location over a 10-year duration are logically grouped into three varying amplitude load cases based on the magnitudes of wind speeds while preserving the accompanying wave loads and percentage occurrence of each. The forces and moments acting on a prototype 10 MW OWT are estimated. Using the relevant scaling laws, an experimental set-up of laboratory offshore wind turbines and loadings are developed and used to perform long term model tests under High Cycle Application loading in sand. Accelerometers and displacement sensors are used to monitor the structural response throughout the experiment. Based on the results, commonly used fixed amplitude cyclic loads may underestimate the change of natural frequencies and/or tilt by up to 20%, with 2% large loads contributing up to 50% of change. This study has the potential to bridge the gap hindering the comprehensive characterisation and prediction of OWT behaviours.

1. Introduction

In bids of modern societies to achieve sustainable and environmentally friendly energy utilisation in their medium to long-term futures, huge interests have been shown in offshore wind turbines (OWTs), making them a popular technology in the global energy industry. For example, Europe and China currently have ambitious targets of achieving 66,488 and 52,000 MW OWT capacities by 2030 (Corbetta et al., 2015; GWEC, 2020). To reach these targeted capacities, the power ratings of the OWT units need to increase from the currently popular 2–5 MW units (Oh et al., 2018) to the recently emergent 8–10 MW units (Desmond et al., 2016) or higher. For these OWTs, the rotor diameters and tower heights must be increased (leading to larger lateral loads and vibration amplitudes) while minimising the overall weight increase to achieve improved power efficiency and a reduced levelised cost of energy, LCOE (Zaaijer, 2006; Shirzadeh et al., 2015; Wiser et al., 2016). The low LCOE of OWTs contributes to their popularity as a megawatt-hour of energy costs cheaper to produce from these assets than nuclear power plants, even as the former catches up to natural gas (Jalbi et al., 2019).

Due to their delicate dynamics, the design of OWTs must satisfy some stringent limit state criteria: ultimate, serviceability and fatigue (ULS, SLS, FLS) (Bhattacharya et al., 2011). To avoid resonance throughout their service lives (typically 25–30 years), DNV (2014) recommends that the fundamental target frequencies of OWTs should be at least ±10% away from 1P (rotor effects due to mass and aerodynamic imbalances)
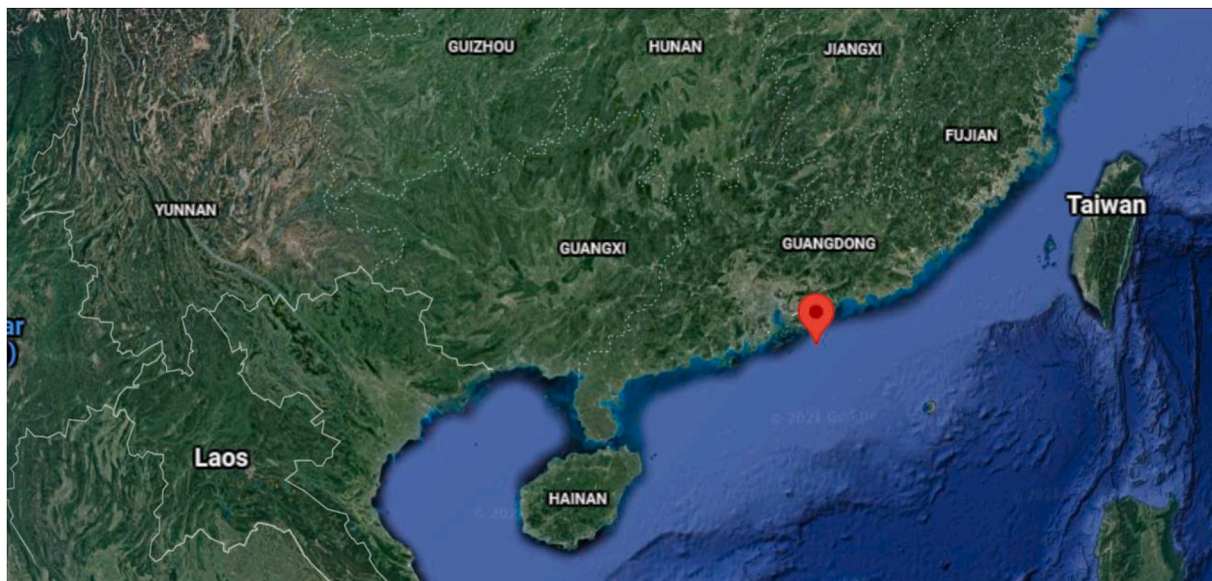

Fig. 1. Sampling location of environmental data.

and 2P/3P (blade passing effects on the tower) frequencies (ULS criterion), leaving three possible positions: less than 1P (soft-soft), between 1P and 3P (soft-stiff), or higher than 3P (stiff-stiff) - with the optimum design position being in the soft-stiff region (Bouzid et al., 2018). However, in this position, the safety band of the OWT natural frequency change is narrow with a tendency for exit (Norén-Cosgriff and Kaynia, 2021). Under the actions of wind, wave, 1P, and 3P, OWTs experience continuous vibrations that change their dynamic foundation fixity conditions and the system's natural frequencies (Kuhn, 2000; Bhattacharya et al., 2011; Guo et al., 2015; Xu et al., 2020). Where the OWT's fundamental frequencies approch those of 1P and 3P, resonance can occur, as in the Areva Multibrid M5000 OWT prototype (Hu et al., 2014). Similarly, such vibrations and loading patterns (asymmetrical due to wind and wave) can cause tilt (rotations) in the OWT foundations, risking the breach of their allowable limits (SLS criterion). For example, monopile and jackets have maximum allowable rotations of $0.5°$, Bisoi and Haldar (2014) and $0.25°$, Zhang et al. (2019) at their sea beds, respectively. Finally, the construction materials of OWTs must be capable of withstanding the repeated cyclic stresses imposed by a large number of cyclic loadings it must endure so as not to reach the fatigue limit of the material (FLS criterion).
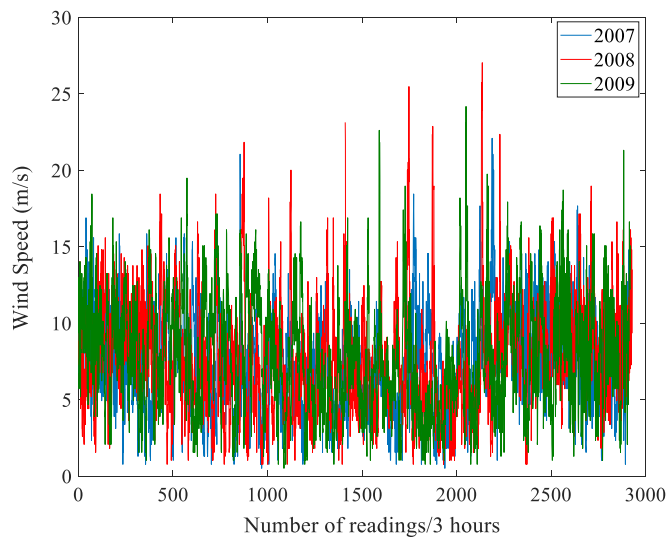
The resulting states of the OWTs following the load applications, may ab-initio, be difficult to accurately characterise or predict due to the strong dependence of the loads on nature. The current practice of OWT condition characterisation and prediction involves collecting and analysing field monitoring data from the structures (Damgaard et al., 2013; Kallehave et al., 2015; Versteijlen et al., 2011; Shirzadeh et al., 2015). However, field challenges, including lack of access to some parts of the OWTs and repeatability difficulties, limit the extents of investigations by such analyses. Therefore, alternative means of characterising and predicting OWT conditions have been sought through scaled model test investigations. With a sufficient amount of information on the environmental loads, prototype OWTs (e.g., Jonkman et al., 2009; Desmond et al., 2016), site soil properties (from laboratory tests), scale models of prototype OWTs can be created, which allows the conduct of controlled model tests. Based on the test results, the conditions of operating OWTs can be characterised, and their behavioural trends can be predicted (Lombardi et al., 2013; Guo et al., 2015; Xu et al., 2020; Abdullahi and Wang, 2021).

The practice of wind and wave load applications to laboratory offshore wind turbines (LOWTs) have evolved. At the onset, an electrodynamic actuator was used to simulate wind and wave loadings on
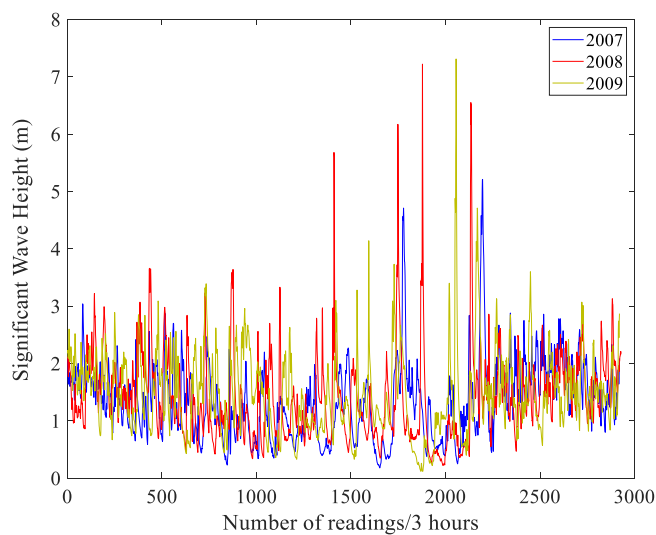
the LOWT (Adhikari and Bhattacharya, 2011; Bhattacharya et al., 2011, 2013). However, this led to inconvenient operations and inevitable human disturbances to the foundation surrounding soil. Guo et al. (2015) and Nikitas et al. (2016) proposed the use of out of balance mass gear systems described in Ewins (2009) on scaled LOWTs to act as both a part of the dead load (representing the rotor nacelle assembly, RNA) and the loading device which addressed the human-soil disturbance challenge. It is noteworthy that in both loading systems mentioned above, the wind and wave loads are simultaneously applied by one excitation device (Lombardi et al., 2013; LeBlanc et al., 2010). Thus, this forces coincident frequency magnitudes and application points for the two loadings, both clear departures from the prototype case. In a bid to address these shortcomings, Yeter et al. (2014); Liang et al. (2020) used two different mass gear balances to apply the wind and wave loads to the LOWTs. The use of two separate mass gear balances located at different positions (hub height and sea level) is employed in this study. They are made to operate at two different frequencies, thereby better preserving the similitude relationship criteria of frequency and cyclic stress ratios between the model and prototype than using one mass gear balance.

Previous research on model tests of OWTs used constant mean load values to represent the loading on an OWT throughout its service life, Adhikari and Bhattacharya (2011); Bhattacharya et al. (2011); Lombardi et al. (2013); Guo et al. (2015); Xu et al., 2020; Abdullahi and Wang (2021). However, this practice does not represent field load applications because both wind and wave loads are known to continuously change magnitudes and directions with time (see Fig. (2) a and b). This warrants the need to investigate the effect(s) of varying amplitude loading regimes, especially High Cycle Application (HCA) ones, on OWTs (as in the prototypes) within the same testing program compared to constant amplitude ones. The study can offer an insight into the contributions of the different load cases (e.g. small, medium or stormy wind conditions) towards reaching the OWT's limit states and the timing (in terms of soil stiffness) of such. For the first time, this study overcomes the challenge of applying a constant mean load value throughout the test by applying three varying amplitude loads per year, culminating in HCA loadings over the 10 considered years. Also, preserving the loading directions on the LOWT as obtained on the prototype is another crucial part of the modelling operation. These are controlled by the wind and wave load excitations (Lombardi et al., 2013). In this study, rose diagrams showing the actual directions of the loadings on the OWT are plotted and replicated on the model.

The objectives of this study are: First, to study the tilt accumulation

a. wind speed time history

b. significant wave height time history

Fig. 2. Typical plots of environmental data (2007–2009).

in OWTs under long term varying amplitude load applications considering the contribution of each load case over the HCA loading duration; Second, to study the natural frequency changes of OWTs under long term varying amplitude load applications considering the contribution of each load case over the HCA loading duration.

To achieve these objectives, a LOWT is designed according to the DTU 10 MW Reference Wind Turbine (Desmond et al., 2016). Considering its popularity and sensitivity to soil stiffness change (Abdullahi et al., 2020), a monopile foundation in sandy deposits is adopted for the study. Experimental investigations into the effect(s) of varying amplitude load applications on the long-term characteristics of OWT is conducted. Long term (10 years) wind and wave-field data sets are used to model the wind and wave loads acting on the prototype OWT which are, in turn, used to get the laboratory-equivalent wind and wave loads acting on the LOWT. The wind loads are categorised into small, mid and large load cases, while their accompanying wave loads, wavelengths and percentage occurrences are preserved. In the first instance, natural frequency and tilt accumulation changes from the application of one-year varying amplitude loadings are compared to those from fixed

Table 1
Simplified wind speeds categorisation.

DTU Wind speed grouping (m/s)	Remark	Present Study Wind speed grouping (m/s)	Remark
4	Cut-in	0–3.9	Small-load case
11.4	Rated	4–11.39	Mid-load case
25	Cut-out	11.4-above	Large-load case

amplitude loadings on the LOWTs. In the second instance, only varying amplitude loadings applied to the LOWT (culminating in HCA loading) are used to study tilt accumulation and natural frequency changes throughout the experiments - being a more realistic representation of natural (operating) loads than average ones.

2. Environmental site data and operating load generation

The adopted site for the prototype OWT in this study lies in the South China Sea (on latitude 22°N and longitude 114.5°E), as shown in Fig. (1). From this site, environmental data (wind speeds, wind directions, significant wave height, wave directions and wave period) recorded at time steps of 3 h for 10 years (2007–2016) were obtained and used to estimate the forces and moments acting on the prototype OWT. Typical plots of the yearly wind speeds and wave heights are shown in Fig. 2 a and b, respectively. The Horns rev wind farm soil profile is adopted for the site because of its similarity to the Red-hill silica sand, which is the typical soil type encountered in the North Sea (Guo et al., 2015) and the seabed along the southeast coastline of China (Wang et al., 2014). A site mean-sea depth of 20 m is adopted for the study (Velarde and Bachynski, 2017).

2.1. Data processing

As questioned earlier, the practice of applying a single force/moment regime to LOWTs in simulating the field loads acting on OWT prototypes does not realistically represent naturally occurring loads on the field. From Fig. 2, the loads are random, alternating between high and low amplitudes. This study attempts to logically categorise these complex loads into forms representing a balance between realistically occurring and laboratory applicable loads. Being the most dominant of the external loads acting on OWTs, Byrne and Houlsby (2003); Jalbi et al. (2019), wind loads (driven by wind speeds) are used for this categorisation. The wind speeds are grouped into small, mid and large load cases for the adopted prototype, as shown in Table 1. This grouping is informed by the popularly adopted wind turbines' manufacturer-wind speed categorisation into cut-in, rated, and cut-out wind speeds, as is the case for the NREL 5 MW, LW 8 MW and DTU 10 MW. The specified wind speeds for the DTU 10 MW wind turbine are 4, 11.4 and 25 m/s for the cut-in, rated, and cut-out cases, respectively. However, since this study investigates the effects of working loads on large OWTs, the equivalents of these wind speeds are specified in ranges based on real environmental data. The three ranges are those below the required speed to cause blade rotations that start electricity production (i.e. before 'cut-in'), those in the range of speeds from when electricity production starts to just before it reaches its optimum (i.e. 'cut-in' to just before 'rated'). The final category describes wind speeds in the range between when electricity production is optimum to when the wind turbine shuts down due to excessive wind speeds beyond the limits it can cope with (i.e. rated to cut-out).

Also, on a close joint interrogation of the wind and wave load amplitudes, it is observed that they are nonlinear; therefore, each wind speed is paired with its uniquely occurring wave data throughout the data processing.

It is important to note that in addition to the loading magnitude of a

Table 2
Load cases and occurrence.

a. simplified varying annual wind speeds			b. simplified varying annual significant wave height			
Year	Small-load case (m/s)	Mid-load case (m/s)	Large-load case (m/s)	Year	Small-load case (m)	Mid-load case (m)	Large-load case (m)
2007	3.448	8.555	16.692	2007	1.255	2.063	4.206
2008	3.473	8.647	18.119	2008	1.364	2.139	4.414
2009	3.443	9.041	17.056	2009	1.373	2.221	3.750
2010	3.594	9.354	16.705	2010	1.115	2.261	3.235
2011	3.625	9.088	17.461	2011	1.343	2.311	5.153
2012	3.413	9.253	17.397	2012	1.389	2.307	4.462
2013	3.267	9.000	17.108	2013	1.379	2.397	4.481
2014	3.365	8.979	16.995	2014	1.392	2.250	5.137
2015	3.579	8.625	17.160	2015	1.401	2.145	4.515
2016	3.430	8.746	13.359	2016	1.338	2.145	4.361

c. percentage occurrence of varying annual			d. simplified varying annual wavelengths wind speeds			
Year	Small-load case (%)	Mid-load case (%)	Large-load case (%)	Year	Small-load case (m)	Mid-load case (m)	Large-load case (m)
2007	24.17	74.28	1.92	2007	47.08	55.67	68.05
2008	25.13	71.54	3.59	2008	48.98	52.23	64.11
2009	25.44	71.13	3.42	2009	57.55	55.53	56.68
2010	14.38	80.20	5.34	2010	50.94	48.12	55.10
2011	20.70	74.24	5.00	2011	55.67	61.62	61.62
2012	20.14	77.00	3.08	2012	57.70	59.29	64.84
2013	23.40	73.90	4.66	2013	57.26	60.45	67.17
2014	25.80	71.16	3.00	2014	58.71	57.55	69.37
2015	24.04	73.50	2.30	2015	63.53	58.57	62.06
2016	26.34	70.50	3.24	2016	52.37	58.42	68.78

certain load case, an OWT's dynamic characteristics also depend on the duration of a particular loading application. Therefore, the field percentage occurrences of the individual load cases are preserved on the LOWT and are used to determine the number of load cycles under each load case in the laboratory. Furthermore, to adequately describe the wave particle motion, the wavelengths for each load case are calculated.

Following Table 1, the annual wind speeds are grouped into their respective load cases, after which their averages are taken. In these groupings, each wind speed is accompanied by its uniquely occurring wave height, where the average of the wave heights in an annual load case represents the wave height for that load case – the same as the wavelengths. Finally, the frequency of occurrence of each load case is expressed as a percentage of the total annual loads to obtain its percentage occurrence. The described groupings of simplified varying wind speeds, wave heights, wavelengths and wind speed percentage occurrences are shown in Table 2 and Fig. 3.

2.2. Wind-wave misalignments

To determine the relative directions of the wind and wave loads on the OWT (alignments/misalignment), their respective discrete direction data are used for the generation of the annual wind and wave rose diagrams for each of the considered ten years, as typically shown in Fig. 4 a and b. With these, the predominant directions in which the loadings act on the OWT are obtained, hence, their alignments relative to each other. Where the two rose diagrams are in the same direction, wind and wave loads are aligned, and their reverse is true otherwise, while the variability of the loading directions determines the extent of misalignment. These alignments are, therefore, preserved in the application of the wind and wave loadings on the LOWT in the laboratory.

2.3. Forces and moments on the prototype OWT

The main forces acting on a typical offshore wind turbine emanate from wind, wave, 1P and 3P loadings. However, only wind and wave are considered here due to their dominant contributions to both the over-turning moments and the long-term tilt of OWTs. The actions of these loads on a typical OWT and their simplified time histories are shown in Fig. 5.

Following Table 1, the frequencies of the forces acting on the prototype OWT are obtained for the respective annual load cases, typical examples of which are shown in Fig. 6 (for the year 2007). It is observed from the plots that the energy content in the wind load lies in the low-frequency region away from the frequencies of the structure (soft-stiff design method) as well as those of the wave load, 1P and 3P. On the other hand, across the three load categories, the wave load frequencies (despite their slight variations) lie close to the structure frequencies and those of 1P and 3P, same as in Arany et al. (2015); Zuo et al. (2018) and Jalbi et al. (2019). The closeness of these frequencies indicates the dynamic nature of the OWT system.

2.3.1. Wind loads on prototype OWT

Following Table 2, the thrust forces, *Th*, acting on the prototype OWT are calculated for each load case across the considered 10-year period. Here, use is made of the general wind load solution following Eq. (1) (Arany et al., 2015).

$$Th = \frac{1}{2}\rho_a A_R C_T U^2 \tag{1}$$

where ρ_a (kg/m^3) represents the air density; A_R (m^2) represents the rotor's swept area; C_T represents the thrust coefficient, while U (m/s) represents the wind speed.

The thrust coefficient C_T (at an assumed constant power output) can be expressed using Eq. (2); where U_R is the turbine rated wind speed.

$$C_T = \frac{3.5(2U_R + 3.5)}{U_R^2} \tag{2}$$

The overturning moment acting at the pile mudline, M_{Th} (Nm) due to the action of the thrust force can be obtained using Eq. (3).

$$M_{Th} = \left(\frac{1}{2}\rho_a A_R C_T U^2\right)(S + H_{hub}) \tag{3}$$

where S (m) is the mean sea depth; and H_{hub} (m) is the prototype hub height.

2.3.2. Wave loads on the prototype OWT

The theory describing the motion of the wave particle is selected based on the met-ocean condition criteria in Dawson (1983). This recommends the linear airy wave theory where the wave heights are small compared to the wavelengths and water depths. Based on Table (2) b (significant wave height) and d (wavelengths), and the water depth (20 m), Velarde and Bachynski (2017), the above condition for the applicability of the linear Airy wave theory is met for this study. Furthermore, 93% of the load cases satisfied the requirements ($\frac{wave\ height}{wavelength}$ Vs $\frac{water\ depth}{wavelength}$) for the linear Airy wave theory deployment, while those outside its recommended deployment zones are represented to accuracy levels of up to 90% and beyond. Readers are referred to Dawson (1983) for more details on these. Based on the foregoing, the linear Airy wave theory is adopted in this study, where Eq. (4) gives the sea surface elevation equation.

$$\eta = \frac{H}{2}cos\left(\frac{2\pi t}{T} - kx\right) \tag{4}$$

where η is the surface elevation; H (m) is the wave height; T (s) is the wave period; k (m^{-1}) is the wavenumber; $\lambda = (m)$ is the wavelength,

a. simplified varying annual wind speeds

b. simplified varying annual significant wave height

c. percentage occurrence of varying annual wind speeds

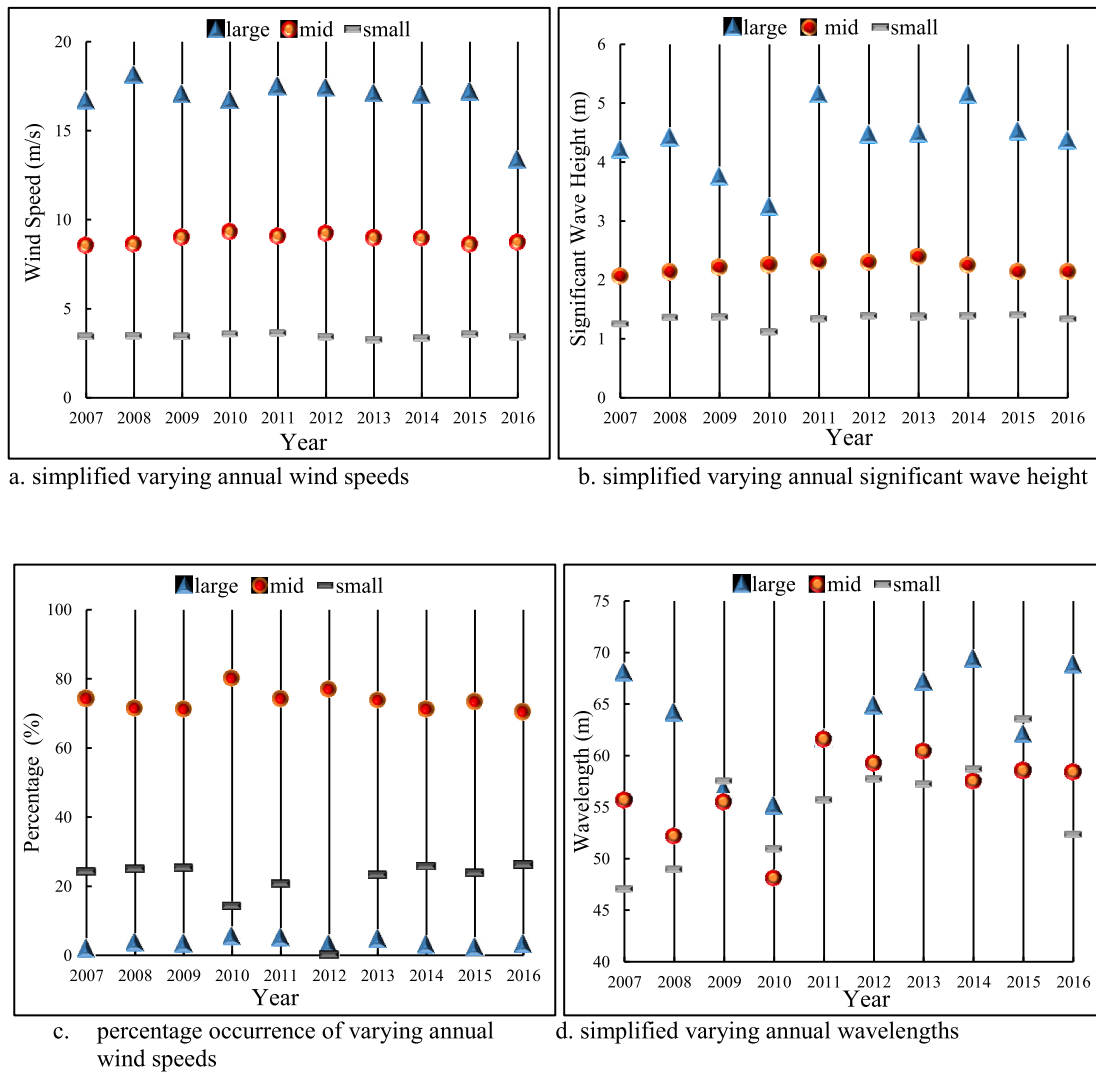d. simplified varying annual wavelengths

Fig. 3. Plots of simplified varying load cases.

while $x(m)$ is the horizontal distance from the pile. The wavenumber, k, and wavelength, λ, can be calculated based on the following equations (Arany et al. (2015); Jalbi et al. (2019) and Bhattacharya (2019).

$$\omega^2 = gk\tanh(kS); \omega = \frac{2\pi}{T}; k = \frac{2\pi}{\lambda} \tag{5}$$

Where $\omega\ (rads^{-1})$ is the angular velocity and $g\ (ms^{-2})$ is the gravitational acceleration.

The selection of the calculation method for the wave load (force) acting on a wholly or semi-immersed monopile is governed by the monopile diameter, D_p and the wavelength, λ, expressed as a ratio, $\frac{D_p}{\lambda}$ (Dawson, 1983; McConnell et al., 2004). Where $\frac{D_p}{\lambda} < 0.2$, the monopile's presence does not strongly disturb the incident wavefield, and the diffraction effects are negligible (McConnell et al., 2004). In such a case, Morison's wave equation is recommended to calculate the wave force (BS6349, 2000; EAU, 1996 and USACE, 2002). Readers are referred to McConnell et al. (2004) for more details. Based on the wavelengths (in Table 2 d) and the 9 m monopile diameter (in Velarde and Bachynski (2017)). In this study, $\frac{D_p}{\lambda}$ ranges between 0.13 and 0.19, hence, the adoption of the Morison's equation for the wave load calculation.

To compute the wave force acting on a unit strip of the submerged pile, dF_{wave}, (N), use is made of Morison's equation in Eq. (6) (Morison et al., 1950).

$$dF_{wave} = dF_D + dF_I = \frac{1}{2}\rho_w D_p C_D w|w| + \frac{1}{4}\pi\rho_w D_p{}^2 C_m \dot{w} \tag{6}$$
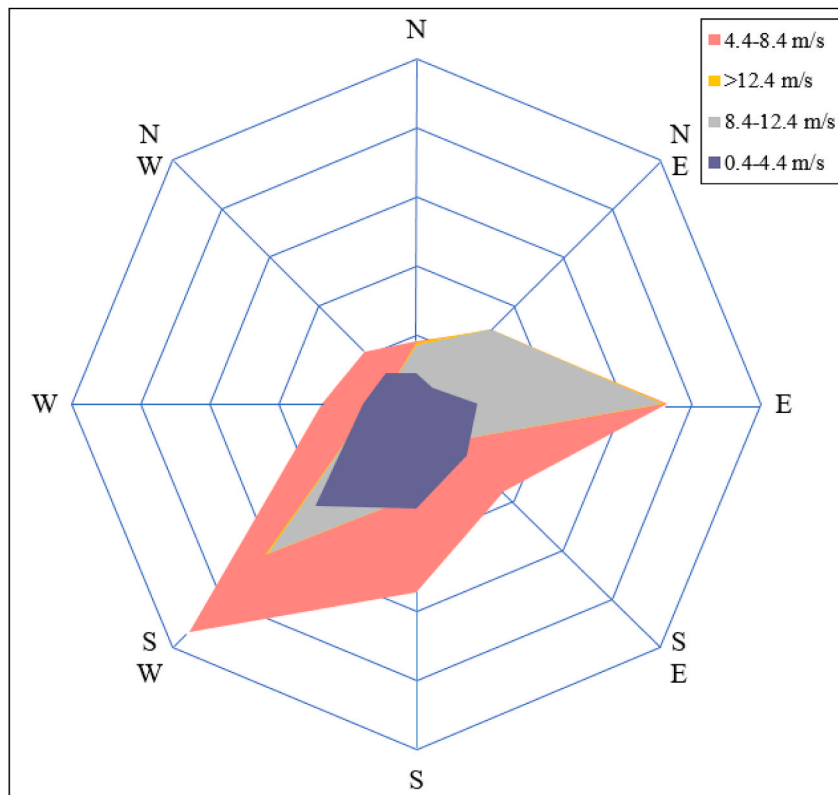
where dF_D and dF_I represent the drag and inertia components of the wave force acting on the strip, respectively. ρ_w is the density of water, C_D and C_m respectively represent the drag and inertia coefficients, while w and $\dot{w}$ represent instantaneous horizontal velocity and acceleration, respectively. C_D and C_m typically range between 0.6 – 1.0 and 1.5–2.0, Dawson (1983), respectively, and for this study, the upper limits of both ranges are adopted (i.e. 1.0–2.0).

To obtain the total horizontal wave force acting on the submerged pile at any time, $t, (s)$ between the elevation surface and mudline (i.e. η to $-S$), Eq. (6) is integrated between these limits to give Eq. (7).

$$F_{wave}(t) = \int_{-S}^{\eta} dF_D dz + \int_{-S}^{\eta} dF_I\, dz \tag{7}$$

It then follows that the wave moment M_wave acting at the mudline of the submerged pile due to the wave force would be a product of Eq. (7) and its lever arm, given by Eq. (8).

$$M_{wave}(t) = \int_{-S}^{\eta} dF_D\,(S+\eta)dz + \int_{-S}^{\eta} dF_I\,(S+\eta)dz \tag{8}$$

a. direction wind rose (2007)

b. direction wave rose (2007)

Fig. 4. Environmental loads direction roses.

Fig. 5. A schematic diagram showing the loads acting on a typical OWT (Bhattacharya et al., 2017).

Considering the time and surface elevations at which the maximum inertia and drag forces occur, their respective definite integrals would lead to the maximum wave forces and their corresponding moments, as shown in Eqs. (9) – (12). The maximum inertia force, F_I,max, and moment, M_I,max, occur at $t = 0$ and $\eta = 0$ while the maximum drag force, F_D,max, and *moment, M_D,max,* occur at $t = T/4$ and $\eta = H/2$ (Jalbi et al., 2019).

$$F_{I,max} = \left[\frac{1}{2}\rho_w D_p^2 C_m \frac{\pi^3 H}{T^2 \sinh(kS)}\right]\left[\frac{\sinh(k(S+h))}{k}\right] \tag{9}$$

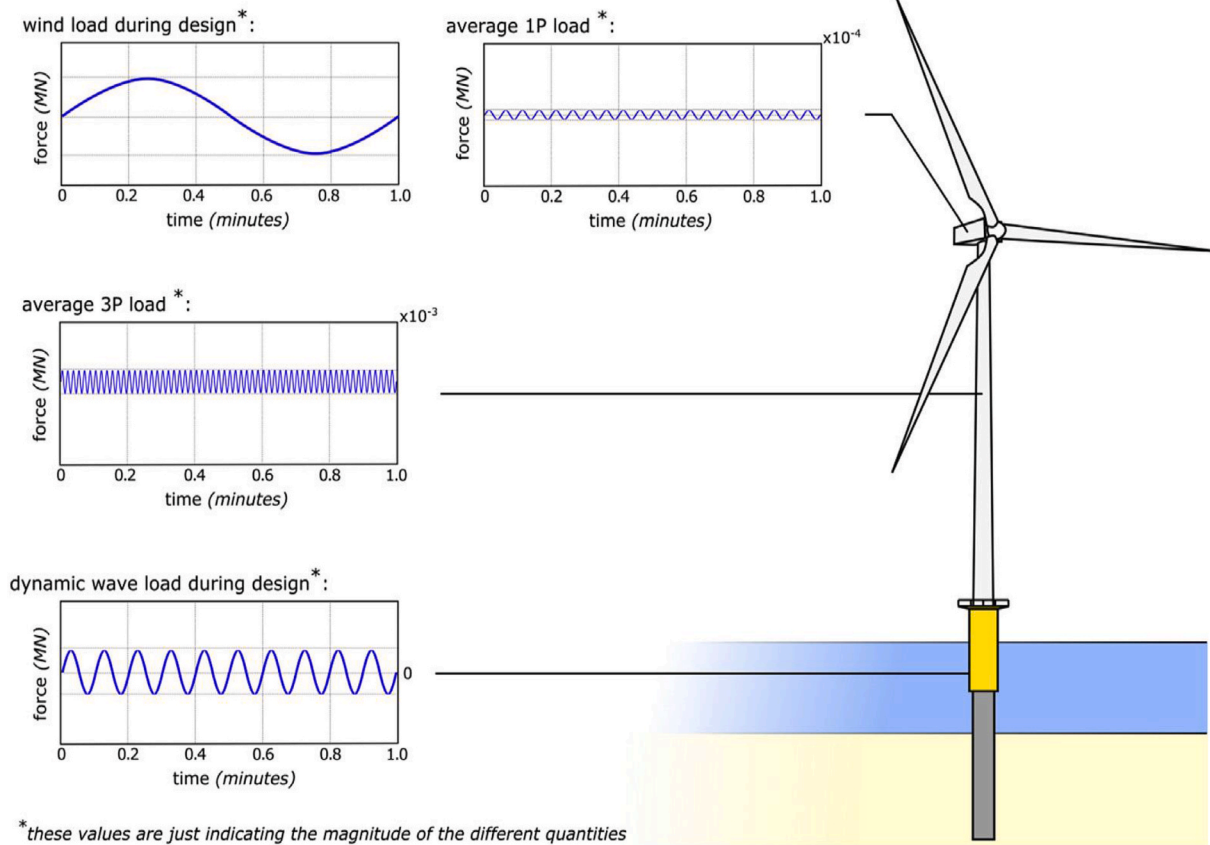$$M_{I,max} = \left[\frac{1}{2}\rho_w D_p^2 C_m \frac{\pi^3 H}{T^2 \sinh(kS)}\right]\left[\left(\frac{S+\eta}{2k} - \frac{1}{2k^2}\right)e^{k(S+\eta)} - \left(\frac{S+\eta}{2k}\right.\right.$$
$$\left.\left. + \frac{1}{2k^2}\right)e^{-k(S+\eta)} + \left(\frac{1}{k}\right)^2\right] \tag{10}$$

$$F_{D,max} = \left[\frac{1}{2}\rho_w D_P C_D \frac{\pi^2 H^2}{T^2 \sinh^2(kS)}\right]\left[\left(\frac{e^{2k(S+\eta)} - e^{-2k(S+\eta)}}{8k}\right) + \frac{S+\eta}{2k}\right] \tag{11}$$

$$M_{D,max} = \left[\frac{1}{2}\rho_w D_P C_D \frac{\pi^2 H^2}{T^2 \sinh^2(kS)}\right]\left[\left(\frac{S+\eta}{8k} - \frac{1}{16k^2}\right)e^{2k(S+\eta)} - \left(\frac{S+\eta}{8k}\right.\right.$$
$$\left.\left. + \frac{1}{16k^2}\right)e^{-2k(S+\eta)} + \left(\frac{S+\eta}{2}\right)^2 + \frac{1}{8k^2}\right] \tag{12}$$

Eqs. (9) – (12) are utilised to obtain the wave load estimates acting on the prototype OWT in this study, where the summation of Eqs. (9) and (11) gives the total maximum horizontal wave force on the pile, while the summation of Eq. (10) and (12) gives the total maximum bending moment at the mudline due to wave action.

Using Eqs. (1) – (3) and (9)–(12), the forces and moments acting on the prototype OWT are computed as shown in Table (3).

3. Experimental studies

The experiments in this study (i.e., model tests on LOWT) aim to investigate the long-term effects of continuously applying varying amplitude HCA loadings to a large OWT supported on a monopile in sand focusing on natural frequency and tilt accumulation changes. Some background details of the testing, including the general methodology and its relation to the Technology Readiness Level (TRL) or validation/ calibration can be found in our recent work, Bhattacharya et al. (2021).

3.1. Similitude relationships

The similitude relationships between the prototype and model OWTs are used to interpret and scale up the experiments to predict the behaviour of the prototypes. Here, the physical processes are expressed as non-dimensional groups, relying on the parameters that control these processes. Therefore, the derivation of the correct scaling laws relevant to the experiment is the study's starting point. The work conducted by Bhattacharya et al. (2011) and Bhattacharya (2019) provides the following parameters and mechanisms, which are relevant to the present study:

1. Geometry and foundation failure mode: A monopile supporting an OWT may exhibit flexible or rigid behaviour during failure, depending on the monopile's slenderness ratio, $\frac{L_p}{D_p}$ (where L_p, is the monopile length and D_p, monopile diameter) and soil stiffness. Where the formation of plastic hinges on the monopile precedes soil plastic failure, the monopile exhibits a flexible failure mode, while in the reverse case, a rocking failure mode occurs (Guo et al., 2015). However, most OWT prototypes would exhibit the latter due to their low $\frac{L_p}{D_p}$ ratio; Other important ratios are the tower slenderness ratio,
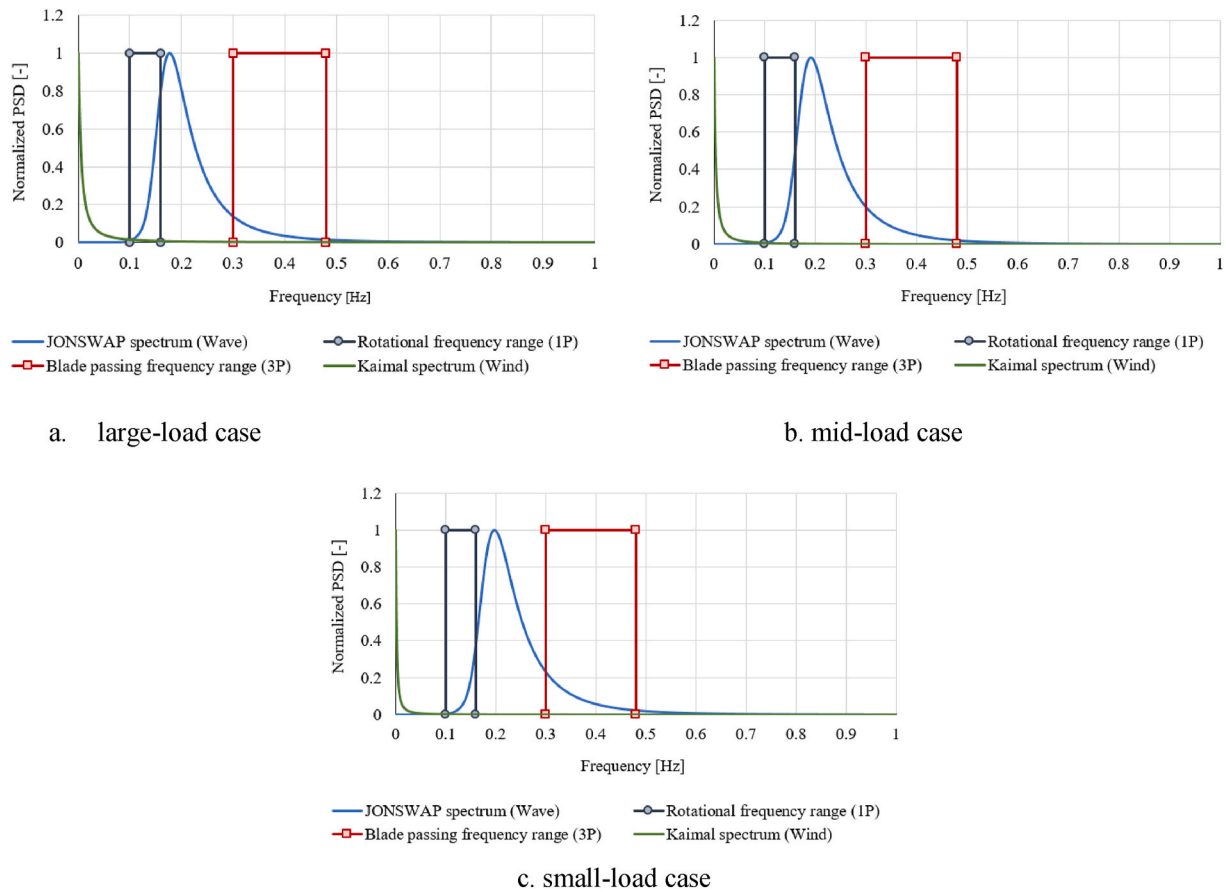
a. large-load case

b. mid-load case

c. small-load case

Fig. 6. Frequency diagrams of different load cases acting on the prototype OWT.

Table (3)
Forces and moments acting on the prototype OWT.

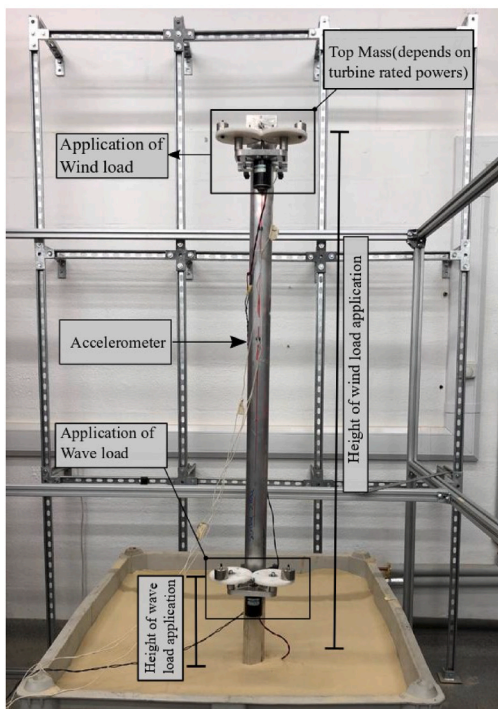| Wind speed (m/s)	Year	$Th(MN)$	$F_{I,max}(MN)$	$F_{D,max}(MN)$	$M_{Th}(MNm)$	$M_{I,max}(MNm)$	$M_{D,max}(MNm)$	$F_{Total}(MN)$	$M_{Total}(MNm)$
16.70	1	1.97	2.55	0.48	274.54	32.24	4.74	5.00	311.52
8.55	1	1.10	1.24	0.09	153.42	15.70	1.05	2.43	170.17
3.45	1	0.56	0.77	0.03	77.38	9.74	0.45	1.36	87.57
18.12	2	2.12	2.53	0.37	295.67	33.21	3.69	5.03	332.57
8.64	2	1.11	1.28	0.10	154.76	16.29	1.16	2.49	172.21
3.47	2	0.55	0.83	0.04	77.38	10.48	0.51	1.42	88.37
17.06	3	2.01	2.20	0.29	279.90	28.28	3.01	4.50	311.19
9.04	3	1.15	1.34	0.10	160.56	16.96	1.25	2.60	178.77
3.44	3	0.55	0.81	0.03	77.23	10.37	0.42	1.40	88.02
16.70	4	1.97	1.90	0.20	274.54	24.42	2.21	4.08	301.17
9.35	4	1.18	1.29	0.11	165.17	16.33	1.32	2.58	182.82
3.60	4	0.57	0.68	0.02	79.61	8.62	0.35	1.28	88.58
17.46	5	2.05	2.75	0.41	285.85	39.89	3.90	5.22	329.64
9.08	5	1.15	1.36	0.10	161.15	17.45	1.16	2.62	179.76
3.62	5	0.57	0.79	0.03	79.91	10.14	0.41	1.39	90.46
17.40	6	2.05	2.50	0.35	284.96	33.72	3.44	4.90	322.12
9.25	6	1.17	1.37	0.10	163.68	17.42	1.21	2.65	182.31
3.41	6	0.55	0.82	0.03	76.78	10.52	0.44	1.40	87.74
17.11	7	2.01	2.45	0.33	280.64	34.14	3.21	4.79	317.99
9.00	7	1.15	1.41	0.11	159.96	18.09	1.24	2.67	179.29
3.27	7	0.53	0.82	0.03	74.70	10.43	0.424	1.39	85.55
16.99	8	2.01	2.75	0.41	278.86	39.57	3.922	5.17	322.35
8.98	8	1.14	1.34	0.10	159.67	17.06	1.189	2.59	177.91
3.36	8	0.54	0.79	0.03	76.04	10.47	0.36	1.36	86.87
17.16	9	2.02	2.55	0.37	281.39	34.12	3.63	4.94	319.14
8.62	9	1.11	1.25	0.08	154.31	16.12	0.961	2.44	171.39
3.58	9	0.57	0.76	0.02	79.31	10.68	0.31	1.35	90.30
13.36	10	1.61	2.39	0.30	224.69	33.39	2.94	4.30	261.02
8.75	10	1.12	1.26	0.08	156.24	16.17	1.01	2.46	173.42
3.43	10	0.56	0.80	0.03	77.08	10.16	0.452	1.39	87.692

Table 4
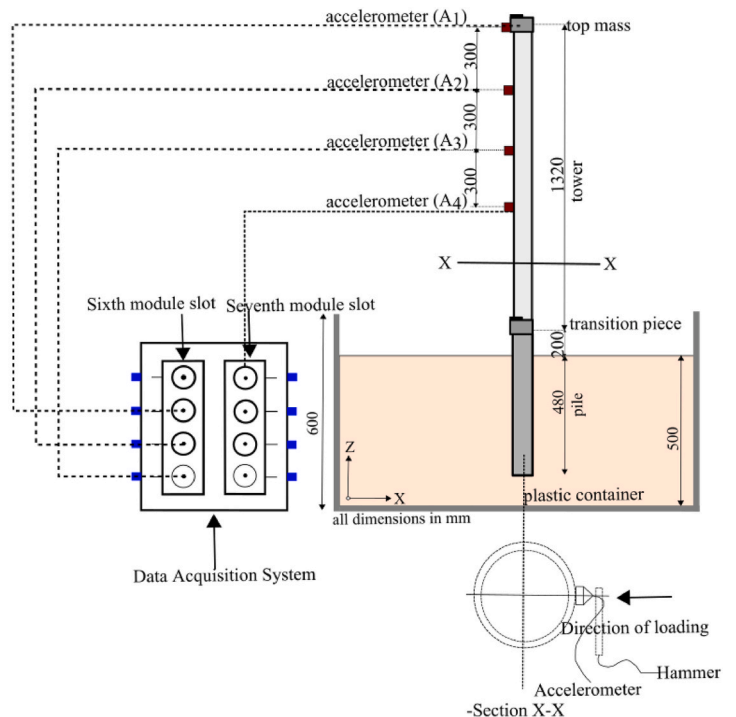Dimensionless groups of models and prototypes.

Dimensionless parameter	Physical model in this study	Physical Model in Guo et al. (2015)	DTU 10 MW OWT sited in Horns-rev Windfarm	PrototypeIn Kentish Windfarm	Prototype in Walney Windfarm
$\frac{h_t}{D_t}$	23.380	23.26	16.750	23.100	26.30
$\frac{L_p}{D_p}$	7.50	8.54	6.110	8.720	8.580
$\frac{h_t}{L_p}$	3.166	2.22	3.302	2.640	3.500
$\frac{M_{Total}}{GD_p{}^3}\,(\times 10^{-3})$	2.070–8.047	0.565–5.926	5.408–21.020	17.10	32.60
$\frac{K_h}{F_f.D_p}\,(\times 10^{-7})$	2198–9709	1630	721–11110	0.0026–0.017	769–2500
$\frac{F_f}{F_n}$	0.060–1.000	0.850–1.300	0.057–0.852	0.37–2.37	0.60–1.94
$m_1:m_2:m_3$	1.43:1.02:1.0	1.88:1.25:1.0	1.70:1.02:1.0	1.3:1.2:1	1.6:1.1:1

Table 5
Geometric and soil properties of the LOWT and some prototypes.

	Physical model in this study	Physical Model in Guo et al. (2015)	DTU 10 MW OWT sited in Horns-rev Windfarm	Prototype in Kentish Windfarm	Prototype in Walney Windfarm
Monopile diameter, D_p (m)	0.064	0.043	9.00	4.30	6.00
Tower diameter, D_t (m)	0.064	0.043	6.90	3.38	4.00
Monopile length, L_p (m)	0.480	0.450	55.00	37.50	51.50
Height of tower, h_t (m)	1.520	1.000	115.60	78.050	105.00
Monopile thickness, P_{th} (cm)	0.028	0.020	3.80	4.50	8.00
Soil type	Sand	Sand	Sand	Sand	Sand
Shear modulus of soil, G, (MPa)	10.000	10.000	21.70	15.950	15.95
Moments (M, Nm)	$(5.68–22.1) \times 10^{-6}$	$(0.5–4.7) \times 10^{-6}$	85.55–332.56	29.02	23.33

a. Photograph

b. schematic representation

Fig. 7. Test set up of the LOWT model.

Fig. 8. Ultimate (pure) moment capacity test set up of the LOWT model.

$\frac{h_t}{D_t}$ (where h_t is the tower height, and D_t, is the tower diameter) and the mass ratios, $m_1 : m_2 : m_3$ between the monopile, tower and RNA. These three ratios constitute the similitude relationships that must be preserved in this group.

2. Strain field in the soil: The amount of stiffness degradation experienced in a particular soil depends on the strain field in the zone of occurrence of an action (e.g. vibration) in that soil. These strains are influenced by the ratio of the soil shear stress to its effective stress at any specific soil depth, known as the cyclic stress ratio, CSR. Bhattacharya et al. (2011) and Lombardi et al. (2013) represented CSR by the non-dimensional group, $\frac{F_{Total}}{GD_p{}^2}$, while Guo et al. (2015) used the non-dimensional group $\frac{M_{Total}}{GD_p{}^3}$, where F_{Total} and M_{Total} represent the total horizontal force and moments acting on the OWT, respectively.

3. Rate of loading: The conditions under which the soil experiences drainage around the monopile are affected by the rate of loading in the soil (Guo et al., 2015). The parameters influencing this are significant pore water pressure generation and dissipation time, t_{gd}, the permeability of the soil, K_h, characteristic monopile length, L_p, monopile diameter, D_p, and forcing frequency, F_f. t_{gd} is directly proportional to D_p and inversely proportional to K_h. t_{gd} is also inversely proportional to F_f. The non-dimensional group responsible for the preservation of the first-order rate of loading relationship is $\frac{K_h}{F_f . D_p}$.

4. Ratios of forcing to system frequencies: This ratio hugely influences the dynamic response of an OWT, and care must be taken to preserve it. The non-dimensional group responsible for the preservation of this relationship is $\frac{F_f}{F_n}$.

Table 6
Properties of the LOWT model.

Component	Length (cm)	Diameter (cm)	Thickness (mm)	Mass (g)
Monopile	48	6.35	2.8	$m_1 = 2427$
Tower	152	6.35	2.8	$m_2 = 2475$
Top mass	–	–	–	$m_3 = 3472$

The non-dimensional parameters of the LOWT and the prototype are listed in Table 4, where the former is geometrically scaled to about 1:80 of the latter. The parameters of the prototype are obtained from Desmond et al. (2016) and Velarde and Bachynski (2017), while those of the physical model in Guo et al. (2015) and prototypes in Kentish and Walney wind farms are obtained from Guo et al. (2015), Jalbi et al. (2019) and Liang et al. (2020), respectively. The non-dimensional groups in this study are very close to the prototype's non-dimensional groups. Reasonably close similarity to the non-dimensional groups in Guo et al. (2015) and the other two listed prototypes are also observed. Detailed parameters of the listed models and prototypes are shown in Table 5.

3.2. Experimental set-up

The LOWT model test was set up and conducted in the Surrey Advanced Geotechnical Engineering (SAGE) laboratory, University of Surrey, UK, as shown in Fig. 7. The set-up was housed inside an aluminium frame that made up the testing space to exclude external tampering-induced vibrations. At the same time, the laboratory

Table 7
Properties of Red-hill silica sand.

Properties	Values
Specific gravity, G_s	2.650
Median particle diameter, D_{50} (mm)	0.120
Angle of internal friction, φ (°)	36.000
Dry unit weight, γ_d	16.800
Maximum void ratio, e_{max}	1.037
Minimum void ratio, e_{min}	0.547
Relative density, D_r	0.630
Shear modulus, G (MPa)	10.000
Uniformity coefficient, C_u	1.630
Horizontal permeability, $K_h \left(\frac{m}{s}\right)$	10^{-4}

temperature was maintained at an average of 24 °C throughout the test. The LOWT model comprises four parts: the monopile and tower (both made of aluminium alloy), the transition piece (doubling also as the wave loading exciter), and the top mass representing the RNA. Fig. 8 shows the ultimate (pure) moment test set-up of the LOWT, while Table 6 shows the parameters of the LOWT model.

The preparation of the sand bed used for the experiment followed a process of releasing Red-hill silica sand into a $60 \times 95 \times 115 \text{ cm}^3$ volume plastic tank from a hopper, at a constant flow rate, until the tank was filled up to about 55 cm. The LOWT model was then driven to a depth of 48 cm into the sand bed, effectively simulating a hinge boundary condition at the monopile tip. The basic properties of the sand are listed in Table 7.

To record the acceleration signals for the model test, four Endevco uniaxial accelerometers were used. The frequency range, sensitivity and model number of these accelerometers are 2500 to 10,000 Hz, $\sim 95 \text{ }mV/ms^{-2}$ and 256–100, respectively. Each accelerometer (weighing 3.5 g) was attached to the LOWT along its vertical axis at 0.5, 30, 60 and 90 cm from the top of the model. Interestingly, each accelerometer mass

constituted only a negligible 0.042% of the model mass, making them incapable of significantly influencing the recorded test signals. The data acquisition process was undertaken, making use of two (of three) four-channel input modules (NI 9234) connected to the National Instrument data acquisition device (DAQ) cDAQ-9178. The four accelerometers were connected to a module channel in the DAQ, starting from the second of the input module in the sixth module slot and filling out the remaining channels with two other accelerometers. The fourth accelerometer was connected to the first channel of the input module in the seventh module slot, while all other channels were left idle. The excitation device used for the impact testing was a modal hammer (No. 2302-5 by Endevco) connected to the first channel of the input module in the sixth module slot. With the DAQ only accurately measuring acceleration signals at sampling frequencies exceeding 3000 Hz, a sampling frequency of 3100 Hz was adopted throughout the experiment. A Lenovo ThinkPad T450 laptop computer was used to visualise, process, and store the acquired data through the National Instrument's Labview interface V18.01f. To record the monopile tilt (rotation), a series connection of displacement measuring equipment consisting of a VL53LOX time-of-flight distance sensor (known here as displacement laser), an Arduino UNO REV3 board, and a recording/visualisation computer (Lenovo ThinkPad T450 laptop) was made. The displacement laser was mounted at a vertical distance of 100 mm from the mudline. The optimum lateral laser sensing distance was 80 mm from the monopile and was adopted throughout the experiment. Fig. 9 shows the photographs of the described test equipment.

3.3. Modelling of the loads acting on the LOWT model by using cyclic loading devices

As shown in Fig. 7, two different mass gear balance systems, one at the top (hub height) and the other just above the mudline (sea level), are used to simulate the wind and wave loads, respectively. Fig. 10 shows the schematic of the mass gear balance, which relies on the concept of centripetal forcing, Ewins (2009), used in Guo et al. (2015); Nikitas et al.
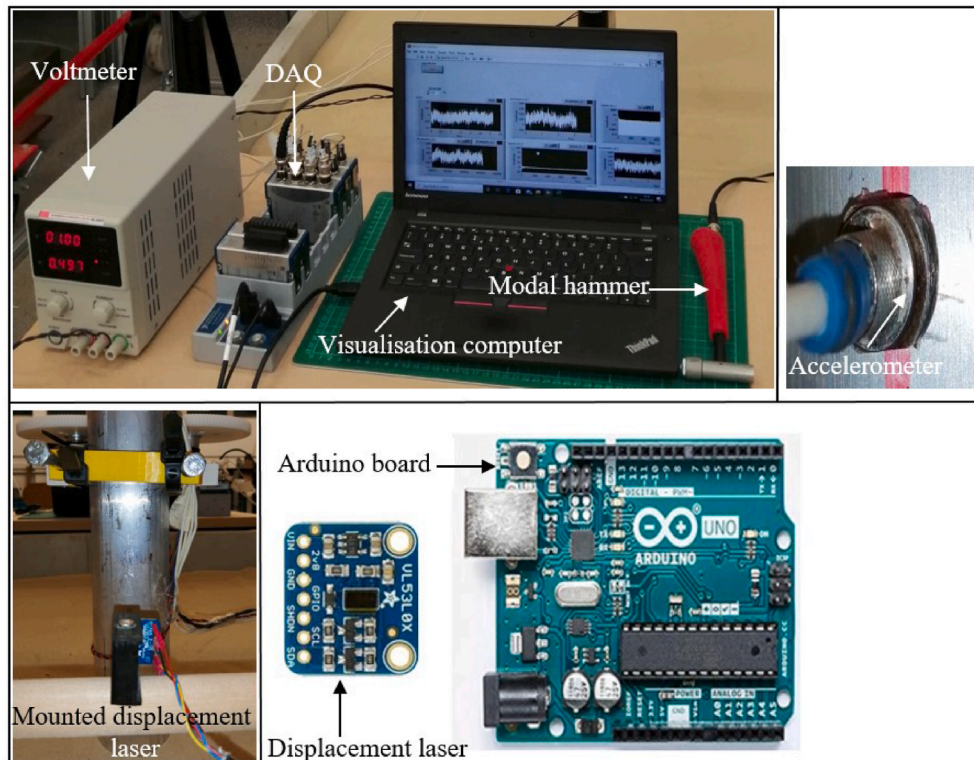

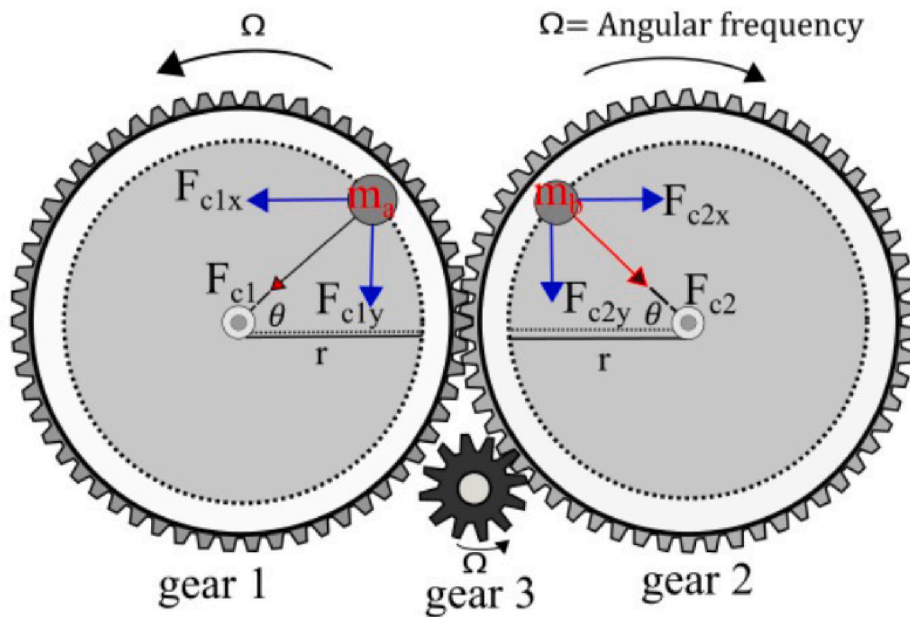**Fig. 9.** Measuring equipment of LOWT model.

Fig. 10a. A mass gear balance system.

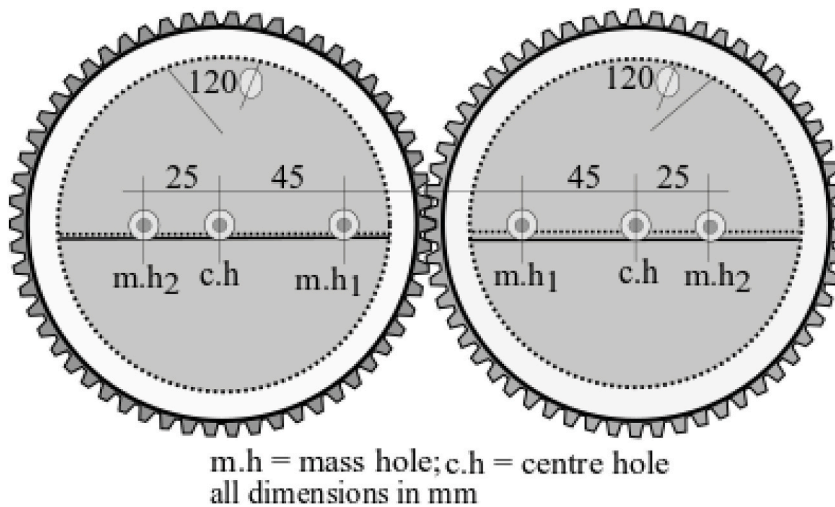

m.h = mass hole; c.h = centre hole
all dimensions in mm

Fig. 10b. Geometric representation of the mass gear balance system.

(2016); and Xu et al. (2020). In this study, a body of mass (m) rotates about a central point at a constant angular frequency (Ω), along a circular arc having a radius (r), thereby producing a centripetal force, F_c (N) as follows:

$$F_c = mr\Omega^2 \tag{13}$$

Each mass gear balance comprises two large eccentric gears, 1 and 2. They have 120 teeth each and a thickness and diameter of 1 and 12 cm, respectively. A third but smaller gear, gear 3, has 12 teeth and a pitch diameter of 1.2 cm. Two equal masses m_a and m_b (kg) are fixed at equal circular arc radii and similar positions on gears 1 and 2, which are in direct contact with each other. Gear 2 is also in direct contact with gear 3, which sits on a direct current (DC) motor (having a rated voltage of 24V and a maximum speed of 6000 RPM), driving it to rotate in an anticlockwise direction, thereby causing gear 2 to rotate in a clockwise direction. In contrast, gear 1 rotates in the opposite anticlockwise direction. This assembly of rotational motions ensures that gears 1 and 2 rotate at equal angular frequencies (Ω), while the resulting centripetal forces from the two gears (on the same device) are F_{c1} and F_{c2}.

Given the equality of the masses, m_a and m_b, the described rotational system shows that the centripetal forces generated by the two gears are due to the contributions of forces in the vertical directions only, which are equal as shown in Eq. (14). Therefore, the total centripetal force, F_{cT}, generated at any particular time is the summation of the individual centripetal forces from the two eccentric gears (Eq. (15)):

$$F_{c1} = F_{c2} \tag{14}$$

$$F_{cT} = F_{c1} + F_{c2} = (m_a + m_b)r\Omega^2 \sin\theta \tag{15}$$

As per Eq. (15), to target a certain centripetal force value, F_{cT}, (N), masses , m_a, m_b (kg) and the rotational circular arc radii , r, can be easily manipulated; while for the angular frequency , Ω, the relationship between the output voltage, v, and device's forcing frequency , F_f(Hz) needs to be established. This requires the calibration of the mass balance gears, which was achieved using a specialised optical tachometer, DT − 2234C$^+$, resulting in the linear equation in Eq. (16):

$$F_f = 2.174v \tag{16}$$

Table 8
Wind and wave annual numbers of load cycles.

Year	Mean wave period (s)	Mean wave frequency (Hz)	Number of cycles	Mean wind period (s)	Mean wind frequency (Hz)	Number of cycles
2007	6.354	0.157	4962916	100	0.01	315360
2008	6.373	0.156	4947741	100	0.01	315360
2009	6.522	0.153	4834725	100	0.01	315360
2010	6.148	0.162	5129393	100	0.01	315360
2011	6.773	0.147	4655814	100	0.01	315360
2012	6.655	0.150	4738564	100	0.01	315360
2013	6.701	0.149	4705841	100	0.01	315360
2014	6.623	0.150	4761391	100	0.01	315360
2015	6.675	0.149	4724039	100	0.01	315360
2016	6.554	0.152	4811546	100	0.01	315360

The modelling of the loads acting on the LOWT model involves three critical aspects: firstly, the determination of the laboratory equivalent loads of the actual prototype OWT loads; second, the manipulation of the mass-balance gear exciters to deliver the equivalent laboratory loads; and thirdly, the determination of the number of equivalent laboratory load cycles that simulate the prototype loadings.

The laboratory equivalent forces/moments are obtained by relying on the similitude relationship governing the loading processes between the model and prototype, namely: the cyclic stress ratio, $\frac{M_{Total}}{GD_p{}^3}$. Here, care is taken to preserve the respective percentage contributions of the wind and wave moments as they occur on the prototype. For example, in the large-load case under the first year, the moment contribution on the prototype due to thrust force was 274.54 MNm, while the wave force contributed 36.98 MNm, amounting to about 88 and 12%, respectively. On the LOWT, similar percentage distribution of these moments (18.2 and 2.5 Nm from the thrust and wave forces, respectively amounting to 88 and 12%) are maintained.

To deliver certain laboratory load equivalents, since the LOWT system mass must be preserved, and the difference between the frequencies of the wind and those of the prototype, wave, 1P and 3P, as shown in Fig. (6) a, b and c, are large, v and r are manipulated to obtain the target F_{Total} and M_{Total} from the simulated wind loads, while m_a and m_b are kept constant. Here, depending on the target force and moment, v values are manipulated by the voltmeter, while r values were alternated on the gears between 25 and 45 mm as shown in Fig. 10b. In contrast, the wave load frequencies are very close to those of the prototype, 1P and 3P, necessitating the preservation of the frequency ratios between the wave load and the prototype OWT on the LOWT system, therefore, only permitting the manipulation of m_a and m_b and/or r values (between 25

and 45 mm) of the wave load mass balance gears to obtain the target F_{Total} and M_{Total}. It is noteworthy that the maximum mass change necessary to reach the target wave loadings constituted only about 0.56% by weight of the LOWT model, thereby being incapable of significantly impacting the system's dynamics. The estimated $\frac{F_f}{F_n}$ values for the prototype are 0.057 and 0.86 for wind and wave, respectively, while corresponding values of 0.06 and 1.0 were adopted as their respective LOWT equivalents.
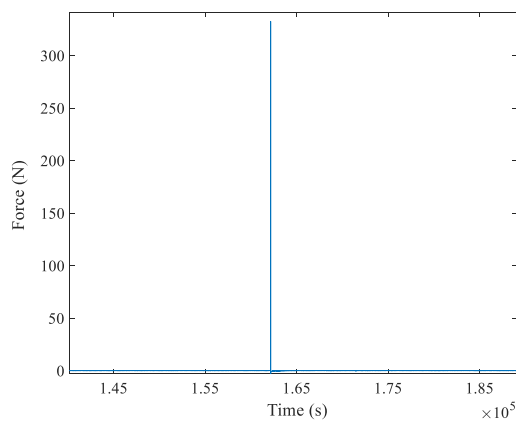
The annual mean wind and wave periods are used to estimate the annual number of load cycles endured by the prototype for the period under review. The inverses of these give the wave frequencies, while the estimate in Arany et al. (2015) is used to obtain the wind frequencies. Table 8 shows these computations per year.
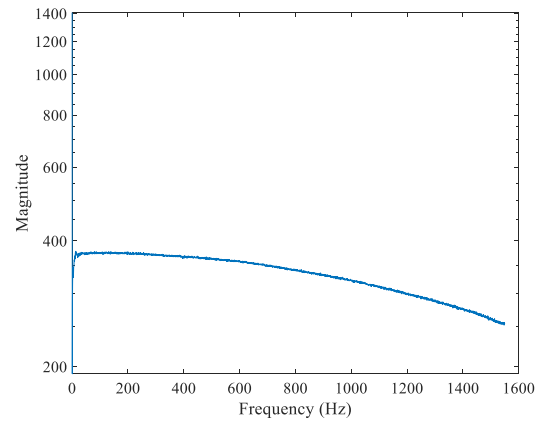
3.4. Modal test

3.4.1. Test procedure

At the outset, the experiment conducted two preliminary investigations. In the first case, the optimum excitation point on the model is determined. This ensures that all nodes of interest simultaneously experience a sufficient level vibration, enough to accurately excite the first two modes the current study relies on. To do this, the model length above the mudline, amounting to about 152 cm, was divided into ten equal parts, with the midpoint of each interval marked for impact. It was found from the time signal visualisation that the optimum impact point satisfying the above condition was around 45 cm from the top and was adopted throughout the study. In the second case, the effect(s) of repeated modal hammer impacts on the natural frequencies of the model is investigated. This precludes any possible influence of the modal hammer impact on the stiffness of the soil surrounding the monopile, and by extension, the frequencies of the model system. To achieve this, 10 modal tests spaced at 30 min apart were conducted on the LOWT model, and the resulting natural frequencies from all the tests were compared. It was found that the natural frequencies remained the same throughout, thereby ruling out the influence of hammer impacts on the soil stiffness and natural frequency of the LOWT system.

Modal tests are conducted in two major stages for the main investigation, before and after cyclic load applications. With the LOWT set-up in place, the model is excited following effective impacts (avoiding 'hammer bounces') from the modal hammer, which is maintained the same throughout the tests, both in position (45 cm from the top) and orientation relative to the normal surface (~90°), following the recommendation of Ewins (2009). The adopted force impulses for the tests are between 300 and 350 N, as shown by a typical excitation-time signal in Fig. 11 a, while Fig. 11 b. shows the frequency-domain signal.

a.   Impact hammer time-domain signal

b. Frequency-domain
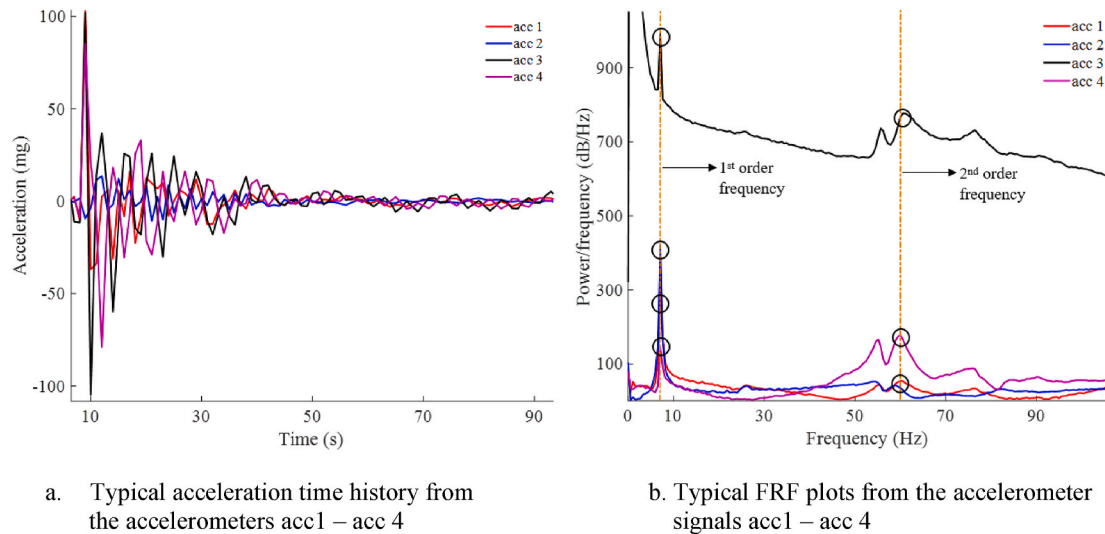
Fig. 11. Impact hammer signals.

a. Typical acceleration time history from the accelerometers acc1 − acc 4

b. Typical FRF plots from the accelerometer signals acc1 − acc 4

Fig. 12. Modal analysis results following the testing.

Table 9
LOWT natural frequencies from different methods.

	Welch Method	Artemis	Difference (%)	FE (ANSYS)	Difference (%)
1st natural frequency	6.990	6.850	2.110	6.843	2.1
2nd natural frequency	57.980	60.124	3.70	62.684	8.1

The latter indicates a frequency band coverage of between 0 and ~1600 Hz, which is half of the specified sampling rate, in line with the Shannon-Nyquist rate of $f_s > 2f_{max}$ (Vlašić and Seršić, 2021). Following the acquisition of the acceleration signals, the first stage of modal testing is completed. The second stage involves conducting a modal test similar to the first after the application of each cyclic loading on the LOWT model. A comparison of the results of the two modal tests shows the changes in the dynamic properties of the system due to the loading. This process is repeated throughout the test.

3.4.2. Modal analysis and validation

Following the acquisition of the vibration signals from the four accelerometers in the test set-up, the time histories and frequency response functions (FRF) of each test case were plotted, typical examples of which are shown in Fig. 12, to allow for the visualisation and assessment of the signal quality. Based on the acceleration data, the modal analysis of the LOWT was conducted using Welch's method (Welch, 1967). The initial modal test results were compared to those obtained from the modal analysis of the same signals using the highly accurate modal analysis software, ARTEMIS, and results from the FE modal analysis of the LOWT (in ANSYS). In these, very close agreements to the Welch's results were recorded (95 and 97%, respectively), thereby validating the test procedure. The first two LOWT natural frequencies from the three methods are as shown in Table 9. Based on Table 1, each of the 10-years' tests was divided into 3 test cases, each comprising 5 excitations and 20 response signals (i.e. 5 excitation x 4 sensors). Consequently, 4 different FRFs were obtained following each excitation; therefore, the FRFs from the 5 excitations were aggregated to obtain the mean FRF at each sensor location for a test case according to the simple formulation by Esu et al. (2021) in Eq. (17).

$$h(f)_j = \left(\frac{\sum_{i-1}^{I} h(f)_i}{I} \right)_j \qquad (17)$$

where, $h(f)_j$ represents the aggregated FRF from a total number of I hits, at the j-th sensor position.

3.5. Testing program

The testing program involves static and cyclic tests as shown in Table 10. Static tests are designated STT, while cyclic tests are CYT. The number following each designation indicates the test order/number, while the letters 's', 'm' and 'l' indicate the small, mid and large load cases, respectively. Similarly, 'PR' represents preliminary and is used to indicate the preliminary cyclic tests, e.g. CYT-PR-1 means preliminary cyclic test one.

Five static tests STT-1 to STT-5, were conducted and used to obtain the moment capacity of the LOWT monopile. Due to the absence of universal guidance regarding the determination of the ultimate capacity of piles, which Liang et al. (2020) attributed to a difficulty in determining the inflexion point necessary to define the monopile failures based on their moment-rotation curves, Byrne et al. (2015) proposed that the ultimate moment capacity of monopiles, M_R, can be taken as the moment causing a monopile rotations, θ_R, of 2 °- which is the ultimate failure criteria and hence, the ULS of the monopile-tower system. To obtain the pure moment, use is made of the Ahmed and Hawlader (2016) proposition which assumes linear $H_R - M_R$ lines for $H_R = 0$; where H_R is the ultimate lateral capacity of the monopile.

On the other hand, the cyclic tests, CYT-1 to CYT-10, constitute the major part of the study, which investigates the long-term behaviour of OWTs considering the effects of loading magnitudes, duration of loadings, and wind-wave misalignments on the tilt accumulation and natural frequency changes of OWTs.
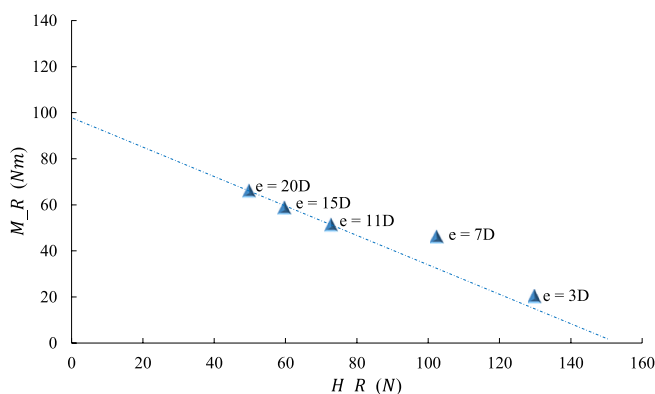
4. Results and discussions

4.1. Static test

Fig. 13 shows the ultimate moment-lateral capacity interaction curve of the LOWT, $H_R - M_R$, for a series of five different eccentricities, e, corresponding to a monopile tilt, θ_R of 2°, Byrne et al. (2015). As stated in section (3.5), the essence of this test is to obtain the ultimate moment capacity of the monopile which will be used as the reference value for the cyclic loading parameters, lv_b used to define the load amplitudes throughout the cyclic tests; where $lv_b = \frac{M_{max}}{M_R}$. The 'pure moment' method proposed by Ahmed and Hawlader (2016) is used to obtain the $H_R - M_R$ curve of the LOWT. From the Figure, the $H_R - M_R$ relationship is linear

Table 10

Testing program.

Test description						
Static tests		Eccentricity (e)				
	STT-1	3D				
	STT-2	7D				
	STT-3	11D				
	STT-4	15D				
	STT-5	20D				
Preliminary cyclic tests		Misalignment (°)	N_1 (wind) $\times 10^5$	M_1 (wind) (Nm)	N_2 (wave) $\times 10^6$	M_2 (wave) (Nm)
	CYT-PR-1	0	3.154	5.142–18.243	4.962	0.598–2.165
	CYT-PR-2	12	3.154	5.142–18.243	4.962	0.598–2.165
	CYT-PR-3	0	3.154	5.142–18.243	4.962	0.598–2.165
	CYT-PR-4	12	3.154	5.142–18.243	4.962	0.598–2.165
Main cyclic test						
	CYT-1-s	0	0.757	5.142	1.191	0.598
	CYT-1-m	0	2.34	10.195	3.672	1.004
	CYT-1-l	0	0.061	18.243	0.099	2.166
	CYT-2-s	0	0.793	5.142	1.237	0.639
	CYT-2-m	0	2.256	10.284	3.562	1.042
	CYT-2-l	0	0.113	19.647	0.199	2.180
	CYT-3-s	12	0.802	5.132	1.209	0.630
	CYT-3-m	12	2.243	10.669	3.433	1.087
	CYT-3-l	12	0.108	18.599	0.145	1.871
	CYT-4-s	0	0.453	5.290	0.718	0.536
	CYT-4-m	0	2.530	10.975	4.104	1.060
	CYT-4-l	0	0.168	18.243	0.256	1.613
	CYT-5-s	0	0.653	5.310	0.978	0.619
	CYT-5-m	0	2.341	10.708	3.445	1.109
	CYT-5-l	0	0.158	18.995	0.233	2.524
	CYT-6-s	0	0.635	5.102	0.948	0.637
	CYT-6-m	0	2.429	10.876	3.649	1.112
	CYT-6-l	0	0.097	18.935	0.142	2.184
	CYT-7-s	12	0.738	4.964	1.082	0.630
	CYT-7-m	12	2.331	10.629	3.482	1.146
	CYT-7-l	12	0.147	18.648	0.235	2.190
	CYT-8-s	0	0.814	5.053	1.238	0.630
	CYT-8-m	0	2.244	10.610	3.381	1.088
	CYT-8-l	0	0.095	18.530	0.143	2.500
	CYT-9-s	0	0.758	5.270	1.134	0.641
	CYT-9-m	0	2.318	10.254	3.496	1.022
	CYT-9-l	0	0.073	18.698	0.144	2.211
	CYT-10-s	0	0.831	5.122	1.251	0.620
	CYT-10-m	0	2.224	10.382	3.417	1.029
	CYT-10-l	0	0.102	14.931	0.144	2.078

Fig. 13. LOWT model $H_R - M_R$ interaction curve for different eccentricities.

between $e = 3D$ and $e = 7D$; the same also applies to $e = 11D$, $e = 15D$ and $e = 20D$ (where $D = 6.35$ cm). It is also observed that as e increases, the lateral force needed to cause a monopile tilt of 2° decreases. The point where the $H_R - M_R$ curve strikes the moment axis is at an approximate M_R value of 96 Nm.

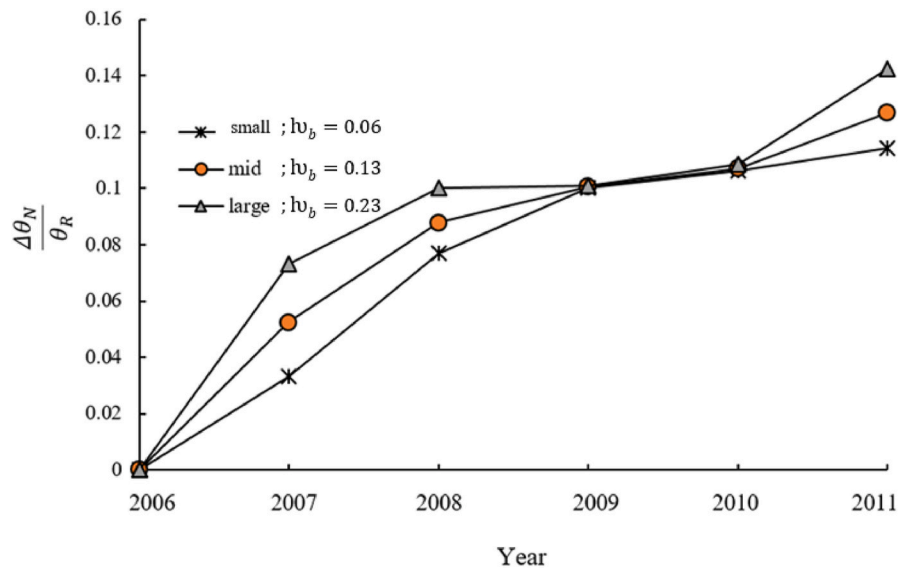### 4.2. Tilt accumulation and natural frequency changes

4.2.1. Preliminary test results

This section presents and discusses the preliminary results for both tilt accumulation and natural frequency changes of the LOWT in the experiment.
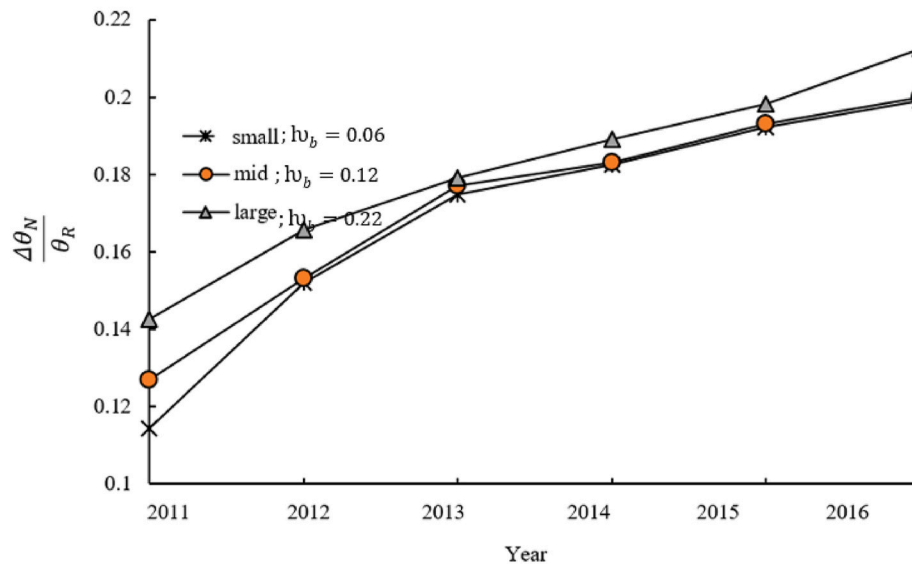
To determine the most effective loading methodology affecting the tilt accumulation phenomenon, the first-year data (i.e., 2007) is used in a preliminary test (CYT-PR-1). In the first instance, the laboratory equivalent of the average (i.e. mean) annual cyclic loading was calculated and applied to the LOWT. Then, its resulting accumulated tilt was measured. In the second instance, the three components of the varying amplitude loadings were sequentially applied to the LOWT (from small through mid, to large-load cases) and the resulting accumulated tilts were measured. The normalised accumulated tilt, $\frac{\Delta \theta_N}{\theta_R}$, from the two respective loading methods are given in Table 11, where $\Delta \theta_N = \theta_N - \theta_o$ (LeBlanc et al., 2010); while θ_N and θ_o are the new and original monopile rotations, respectively. Comparing the tilts from the two loading methods, it can be observed that a higher monopile rotation occurred under the varying amplitude loading method than the constant average amplitude loading method, suggesting an underestimation of the LOWT tilt by the latter. Such underestimations can reach substantial amounts (in this case, up to 4%). The former is therefore adopted throughout the experiment; where θ_R values of 0.5 and 2° are adopted as the SLS and ULS monopile rotation criteria, respectively. Further, the effect of

Table 11

Frequency/Tilt-change difference based on the loading method.

	before loading	after one-year average loading	After 1st year varying loadings $+0°$ misalignment	after 1st year varying loadings $+12°$ misalignment
1st $\frac{F_n}{F_{n-ini}}$	1.0	1.028	1.036	1.034
2nd $\frac{F_n}{F_{n-ini}}$	1.0	1.119	1.122	1.121
$\frac{\Delta\theta_N}{\theta_R}$	0	0.050	0.052	0.050

a. Progression of pile tilt over the first five years

b. Progression of pile tilt over the second five years

Fig. 14. Tilt accumulation of the LOWT under varying amplitude loading.

wind-wave misalignment on the accumulated monopile tilt was equally investigated in the second preliminary tilt test (CYT-PR-2). Here, a 12° wind-wave misalignment was introduced to the LOWT model under similar varying amplitude loadings to the one described above, and the accumulated monopile tilt was measured, as shown in Table 11. It can be observed that the accumulated tilt was slightly higher under a loading misalignment of 0° compared to that of 12° (the difference being 4%).

This suggests that loading misalignments have a reduction effect on the accumulation of monopile tilts, and ignoring such where they occur, can result in the overestimation of the LOWT tilts – depending on the loading magnitude and the degree of misalignment. Therefore, the annual loading misalignments are considered in this study where they occur as reflected by their respective wind and wave rose diagrams.

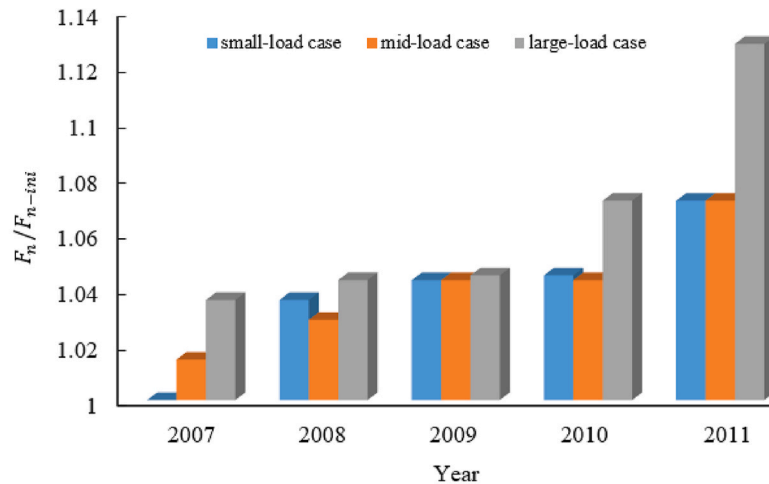To determine the best loading method for the investigation of the

Table 12
Tilt accumulation of the LOWT under varying amplitude loading.

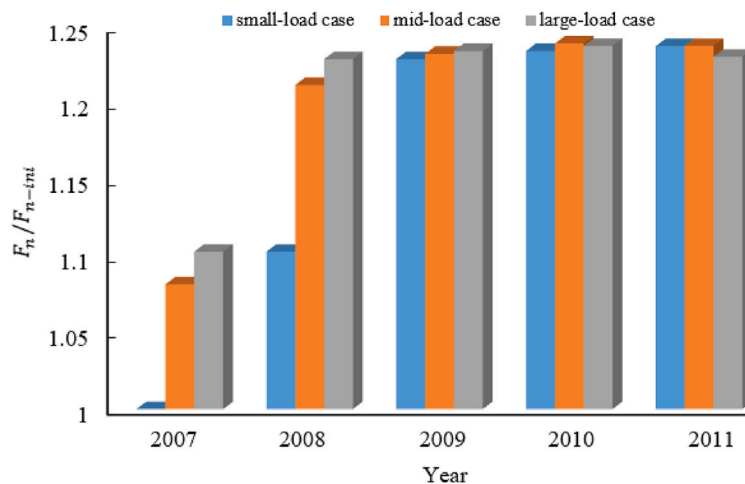| Year	small-load case	mid-load case	large-load case
2006	0	0	0
2007	0.033	0.052	0.073
2008	0.077	0.088	0.100
2009	0.100	0.101	0.101
2010	0.104	0.107	0.109
2011	0.114	0.127	0.143
2012	0.152	0.153	0.166
2013	0.175	0.177	0.179
2014	0.182	0.183	0.189
2015	0.192	0.193	0.198
2016	0.199	0.200	0.213

change in the LOWT natural frequencies, the normalised first-year LOWT natural frequency changes, $\frac{F_n}{F_{n-ini}}$ after applying varying amplitude loadings are compared to those following fixed (i.e. average) amplitude loadings (CYT-PR-3) as shown in Table 11. Where $\frac{F_n}{F_{n-ini}}$ represents the ratio of the natural frequency after cyclic loadings to its initial natural frequency. It can be seen that larger frequency changes occurred (across the first two orders) under the varying amplitude

loadings compared to the fixed amplitude loading. This implies that the commonly used fixed amplitude loading method may underestimate the changes of natural frequencies of the LOWT by substantial amounts (in this case, by close to 30%), which may affect the quality of the test results. Considering the closeness of the former to the real case on the field, it is adopted throughout the experiment. Similarly, the effects of wind-wave misalignment on the natural frequency change of OWTs (CYT-PR-4) were investigated. Table 11 also shows the comparisons of the natural frequency changes of the LOWT between aligned and misaligned wind-wave loads after applying the first-year varying amplitude loading. It can be seen that higher natural frequency changes were recorded (across the first two orders) in the aligned loading cases compared to the misaligned ones (with the difference reaching 5.5%). Therefore, the annual loading misalignments are considered where they occur in the frequency change investigations as reflected by their respective wind and wave rose diagrams.

In general, from Table 11, the average underestimation of the LOWT natural frequency changes and tilt accumulations under the fixed amplitude loading was 19.8% (~20%). Therefore, to guarantee the quality of the LOWT model tests in predicting the behavioural trend patterns of their prototype OWTs, the adopted loading methodology and misalignments on the LOWT must be as close to that of the field cases as

a. First-order natural frequency changes for the first five years ($F_{n-ini} = 6.99\ Hz$)

b. Second-order natural frequency changes for the first five years ($F_{n-ini} = 57.98\ Hz$)

Fig. 15. Contributions of the load cases to changes in the LOWT natural frequency.

possible, because these substantially affect the test results.

4.2.2. Main test results

For the primary investigations into the accumulated monopile tilt and natural frequency changes in OWTs under HCA loadings, cyclic tests, CYT-1 to CYT-10, were conducted on the LOWT. The results are presented and discussed below.

For the monopile tilt accumulation, the individual tilt contributions from the annual load cases were measured throughout the tests, as shown in Fig. 14 and Table 12. At a given time, to obtain the monopile tilt, the lateral monopile displacement resulting from applying a load case (which was opposite to the angle of monopile rotation) was calculated as the difference between the monopile displacements before and after the load application. Therefore, by considering the vertical distance of the point of action of the displacement laser on the monopile from the bottom monopile tip and the lateral displacement of the former, the monopile rotation angle was trigonometrically obtained. This procedure was repeated after each load case application (i.e. three such readings per year). Across the first two years which signalled early loading time, all the three load cases made substantial contributions to the accumulated monopile tilt due to the loose nature of the freshly laid sandbed. However, as the number of load cycles increased with time into the third and fourth years, a more pronounced migration of soil particles occurred from the top to the bottom layers, leading to the densification of the soil surrounding the monopile. This, thus, reduced the monopile's degree of freedom and caused the individual contributions from all the three load cases to wane. However, between the fifth and the tenth year, the large-load case contributed the most significant share of the accumulated monopile tilt due to its ability to expand previously densified soil zones (otherwise known as subsidence zones), whose progressions are shown in Fig. 17. The described trend is very obvious from Fig. 14 b, where a clear consistent departure is observed between the curves of the large-load and those of the small and mid-load cases, respectively. This means that despite only marginally occurring (~2%), the large-load-case contributed the most to the accumulation of the monopile tilt (~50% of the total); the mid-load-case, with a percentage occurrence of about 74%, contributed an accumulated monopile tilt of about 27% of the total. In contrast, with a percentage occurrence of about 24%, the small-load case contributed an accumulated monopile tilt of about 23% of the total. This indicates that as well as the number of cyclic loads, the loading amplitude also significantly affects the amount of tilt a monopile accumulates under cyclic loading, with the latter contributing more to the phenomenon.

From the result, it can be deduced that tilt accumulations can be caused by any load-case between the onset and end of second year loading. However, the extent of tilt is proportional to the loading magnitude. In the subsequent years of loading, however, the large load cases would account for most of the soil densifications and tilt accumulations experienced by the OWT. The ensuing subsidence zones created are largely expandable only by equal or higher magnitude loadings, explaining why small and mid-load cases had very little influence on tilt accumulation in those years. Furthermore, where a fixed amplitude loading is applied to the LOWT, very little tilt would be observed beyond its created zone of influence (subsidence), hence the erroneous popular notion that the accumulation of tilt is primarily controlled by loading cycle number. By comparing the tilt contributions from the first and tenth year loads across the three load cases, the former is found to be more influential than the latter because the rate of increase of monopile tilt decreases with soil densification.

For the primary investigation into the natural frequency change of the LOWT system, the first order LOWT $\frac{F_n}{F_{n-ini}}$ changes for successive application of the load cases in tests CYT-1 to CYT-5 are shown in Fig. 15 a., while Fig. 15 b. shows the second order $\frac{F_n}{F_{n-ini}}$ changes. For the rest of the article, the cyclic stress ratio – load cycle percentage pairs for each loading case are designated as 'CL: cyclic stress ratio value-load cycle

percentage value of total loads' (for example, CL: 2.12×10^{-3}- 24.17% for CYT-1-s represents CSR (2.12×10^{-3}) applied for about 24.17% of the total wind and wave loads cycle numbers).

In the test CYT-1-s (CL: 2.12×10^{-3}- 24.17%), the first-order frequency remained unchanged while the second-order increased by about 1.72%. This is because the applied loading caused only small amplitude vibrations in the tower-monopile system, thereby only partially reducing the voids in the loosely prepared sand bed despite a relatively high loading cycle number, which is similar to the results in Guo et al. (2015); Liang et al. (2020). It is also evident that the second-order natural frequency was able to track the slight change in soil stiffness where the first-order frequency failed, indicating a higher sensitivity of the former to onset soil stiffness changes. In the test CYT-1-m (CL: 4.12×10^{-3}-74.28%), however, due to relatively higher CSR and application cycle numbers, increases in both the first and second-order frequencies were observed, amounting to about 1.46 and 10.03%, respectively. These changes can be attributed to both larger vibration amplitudes of the tower-monopile system and HCA. The combination of the two factors above caused a more pronounced reduction of the sand voids, leading to the densification of the soil and a reduction of the degree of freedom of the monopile-soil system. The result further stresses the higher sensitivity of second-order frequencies to onset soil stiffness changes than first-orders. In the test CYT-1-l (CL: $7.54 \times 10^{-3} - 1.92\%$), which had the largest CSR and the smallest application cycle numbers of the three load cases, the first and second-order frequencies increased by 3.6 and 12.2%, respectively. This indicates a substantial void reduction in the soil surrounding the monopile and a consequent reduction in the monopile's degree of freedom. Therefore, considering this behaviour vis-à-vis that from the preceding CYT-1-m test, it can be deduced that soil stiffness and natural frequency changes of OWT systems are affected more by the magnitude of the tower-monopile vibration amplitude than the applied number of cyclic loads. This explains the stronger influence of soil stiffness increase over degradation in the system's observed net soil stiffness change.

In the test CYT-2-s (CL: 2.14×10^{-3}- 25.13%), the first and second-order frequencies remained unchanged, indicating that the sand voids had been filled beyond the influence zone of the test's loading, hence, making it impossible for the soil stiffness to undergo any further changes; however, in the test CYT-2-m (CL: 4.17×10^{-3}- 71.54%), both order-frequencies recorded changes, with the cumulative first dropping to an increase of 2.89% while the second increased to 23%. This indicates that the combined effects of the vibration amplitudes and load cycle numbers were large enough to exit the previously formed influence zone, creating a new and larger one (developed subsidence zone) in the sand, as shown in Fig. 17. This has a scouring effect on the upper part of the monopile in contact with the soil while recording increased densification in the parts of the monopile in contact with the soil. In the tests CYT-2-l (CL: 8.05×10^{-3}- 3.59%) the first and second-order natural frequencies increased to 4.32 and 25.03%, indicating further soil densification similar to that described in CYT-2-m.

Interestingly, neither test CYT-3-s (CL: 2.13×10^{-3}–25.44%) nor CYT-3-m (CL: 4.33×10^{-3}- 71.13%) were able to change either of the first and second-order frequencies of the system from their previous states, similar to the case in test CYT-2-s. Additionally, the simulated 12% wind-wave misalignment may have reduced the loading vibration effect on the soil by localising this to the tower-monopile system; upon the conduct of CYT-3-l (CL: 8.05×10^{-3}- 3.59%); however, the first and second-order frequencies increased marginally to amounts of 4.49 and 25.04%, respectively, indicating the beginning of the expansion of the influence zone. Tests CYT-4-s (ML: 2.14×10^{-3}–14.38%) and CYT-4-m (CL: 4.42×10^{-3}–80.20%) exhibited similar behaviours to their CYT-3 counterparts in the sense that both first and second-order frequencies remained unchanged from their last values, while in test CYT-4-l (ML: 7.29×10^{-3}–5.34%), the first natural frequency increased to 6.69% and the second to 25.91% (the maximum recorded throughout the test).
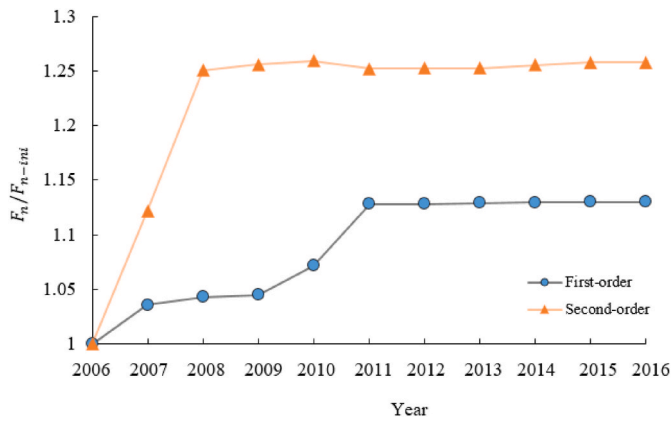
Fig. 16. First and second-order natural frequency changes.

The trend of natural frequency changes suggests that second-order frequencies are more sensitive to onset soil stiffness changes than later ones, while the reverse is true for first-order frequencies. The soil stiffness changes reached their maximum in test CYT-5-l (ML: 7.98 × 10^{-3}–5.00%) where the first-order frequency change increased to 12.75% (the maximum recorded throughout the test) while the cumulative second-order frequency dropped to 25.4% from its previous value. In the tests CYT-6 and CYT-7, the first and second-order natural frequencies show a continuous decline, stabilising somewhat in the test CYT-8 and throughout the test, as shown in Fig. 16. This decline in natural frequencies can be attributed to the heavy subsidence experienced by the monopile as studied by Cuéllar et al. (2009), the progression of which is shown in Fig. 17. Summarily, the magnitude of vibration amplitude contributed more to soil stiffness than the number of load cycles. This is obvious for example, considering that the timing/occurrence of stormy weather would determine how quickly an OWT might

reach resonance.

In general, through the entire experiment involving HCA loadings on the LOWT, although the occurrence of the large loads was only about 2% of the total cyclic loads, it contributed up to 57% of the change of natural frequencies of the LOWT, while the mid and small-load cases contributed 41 and 2% respectively.

5. Conclusions

In this paper, the long term effect(s) of operating loads on large monopile-supported offshore wind turbines in sandy deposits are studied. Environmental data obtained from the proposed OWT prototype location collected over a 10-year period are logically grouped into three different load cases based on the magnitudes of the wind speeds while preserving the percentage occurrence of each; based on these, the forces and moments acting on the prototype OWT are estimated. Using the relevant scaling laws, an experimental set-up of the laboratory OWT is developed and used for scaled long term model tests. The effect(s) of the described system of loadings on the accumulated monopile tilt and natural frequencies of OWTs are investigated. Based on the test results, the following conclusions can be drawn:

1. Tilt accumulations in monopile supported OWTs in sandy deposits increase with load cycles and loading amplitudes, with the latter being more influential. Even if only nominally applied (in this case, 2% of total), the large load cases contribute most to the phenomenon (here, by up to 50% of the total). In contrast, the assumption of constant amplitude loadings can underestimate tilt accumulation estimates in OWTs' characterisation studies. In general, tilt accumulations are more noticeable in soils around freshly installed monopiles; the accumulation rate reduces when soil stiffness increases under continued loading.
2. The natural frequencies of monopile supported OWTs in sandy deposits increase with load cycles and loading amplitudes until the
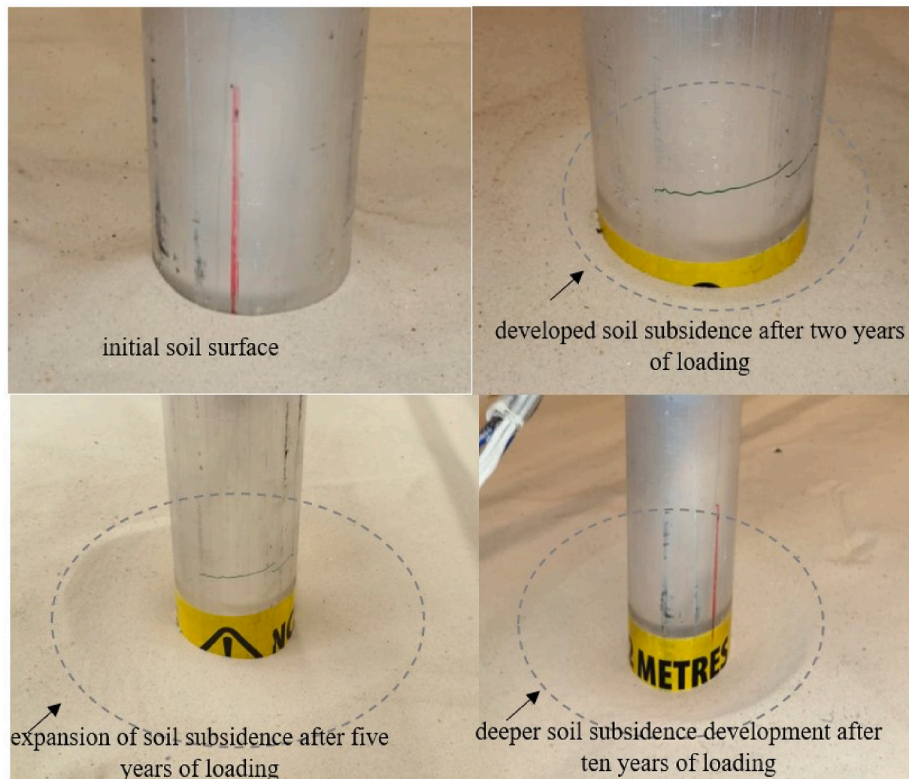

Fig. 17. Soil subsidence development with cyclic loading.

maximum load case influence zone is reached. Similar to tilt accumulation, the loading magnitudes have higher influences on natural frequency changes than load cycles as evidenced by the effect of the large load case (applied for only 2% of total loading time) accounting for 57% of the total changes. Notably, the second-order natural frequency seems to be more sensitive to onset soil stiffness changes. Since all the observed natural frequency changes are positive, it is recommended that the target fundamental natural frequencies be situated close to the upper limit of 1P frequency (see Fig. 6) to reduce the OWT's susceptibility to resonance.

3. If average constant amplitude loadings are used, both increments of tilt accumulations and natural frequencies will be underestimated (in this case, by up to 20%). The percentage underestimations are proportional to the differences in magnitude and number of cycles between the large load case and the average load case. Furthermore, under the condition of equal amplitude loadings, wind-wave misalignment slightly reduces the increments of the natural frequency and tilt accumulation. Therefore, the loading simulation must be carefully considered for future tests in the laboratory.

Future research efforts can be placed on the following:

1. The conclusions above are reached based on red-hill silica sand, having a relative density of 0.630. Other kinds of soils (including cohesive soils) with different parameters are recommended for future studies under a similar kind of loading methodology as proposed in this paper.

2. The current study is based on the 10-years environmental load from the proposed prototype site location and is not representative of all load types across other wind farms (usually spanning between 25 and 30 years). Future studies using a wider range of site-specific environmental loads spanning up to 25–30 years from other locations are recommended to gain more insight into general OWT behaviours.

3. It is important to mention that the results of the scale model tests in this study cannot simply be scaled up to get the actual responses of its OWT prototypes. Rather, the observed trends show the expected behaviour of the prototype. Details of scaling, do's and don't's can be found in Bhattacharya et al. (2021a, 2021b). In the same vein, the dry sand used in the study is based on the assumption that the pore water pressure accumulation in offshore sand is negligible. Therefore, a comparative study between the dry and saturated soil embedded monopile under a similar loading methodology is recommended for future studies.

CRediT authorship contribution statement

Aliyu Abdullahi: Methodology, Investigation, Formal analysis, Visualization, Writing – original draft. **Subhamoy Bhattacharya:** Validation, Resources, Writing – review & editing. **Chao Li:** Resources. **Yiqing Xiao:** Resources. **Ying Wang:** Supervision, Conceptualization, Validation, Resources, Writing – review & editing.

Declaration of competing interest

The authors declare that they have no known competing financial interests or personal relationships that could have appeared to influence the work reported in this paper.

References

Abdullahi, A., Wang, Y., 2021. June). Digital twin-like model updating of a laboratory offshore wind turbine with few-parameters soil-structure interaction model. In: SHMII-10 2021-10 International Conference on Structural Health Monitoring of Intelligent Infrastructure.

Abdullahi, A., Wang, Y., Bhattacharya, S., 2020. Comparative modal analysis of monopile and jacket supported offshore wind turbines including soil-structure interaction. Int. J. Struct. Stabil. Dynam. 20 (10), 2042016.

Adhikari, S., Bhattacharya, S., 2011. Vibrations of wind-turbines considering soil-structure interaction. Wind Struct. 14 (2), 85.

Ahmed, S.S., Hawlader, B., 2016. Numerical analysis of large-diameter monopiles in dense sand supporting offshore wind turbines. Int. J. GeoMech. 16 (5), 04016018.

Arany, L., Bhattacharya, S., Macdonald, J., Hogan, S.J., 2015. Simplified critical mudline bending moment spectra of offshore wind turbine support structures. Wind Energy 18 (12), 2171–2197.

Bhattacharya, S., 2019. Design of Foundations for Offshore Wind Turbines. John Wiley & Sons.

Bhattacharya, S., Lombardi, D., Muir Wood, D., 2011. Similitude relationships for physical modelling of monopile-supported offshore wind turbines. Int. J. Phys. Model. Geotech. 11 (2), 58–68.

Bhattacharya, S., Cox, J.A., Lombardi, D., Muir Wood, D., 2013. Dynamics of offshore wind turbines supported on two foundations. Proc. Inst. Civil Eng. Geotech. Eng. 166 (2), 159–169.

Bhattacharya, S., Nikitas, G., Arany, L., Nikitas, N., 2017. Soil-Structure Interactions (SSI) for offshore wind turbines. IET eng. Technol. Ref. 24 (16).

Bhattacharya, S., Lombardi, D., Amani, S., Aleem, M., Prakhya, G., Adhikari, S., et al., 2021a. Physical modelling of offshore wind turbine foundations for TRL (technology readiness level) studies. J. Mar. Sci. Eng. 9 (6), 589.

Bhattacharya, S., Demirci, H.E., Nikitas, G., Prakhya, G.K.V., Lombardi, D., Alexander, N. A., Aleem, M., Amani, S., Mylonakis, G., 2021b. Physical modelling of interaction problems in geotechnical engineering. In: Modeling in Geotechnical Engineering. Academic Press, pp. 205–256.

Bisoi, S., Haldar, S., 2014. Dynamic analysis of offshore wind turbine in clay considering soil–monopile–tower interaction. Soil Dynam. Earthq. Eng. 63, 19–35.

Bouzid, D.A., Bhattacharya, S., Otsmane, L., 2018. Assessment of natural frequency of installed offshore wind turbines using nonlinear finite element model considering soil-monopile interaction. J. Rock Mech. Geotech. Eng. 10 (2), 333–346.

British Standards Institution, 2000. *British Standard Code of Practice for Maritime Structures, Part I: General Criteria.* BS 6349. Part 1: 2000 (and Amendments 5488 and 5942). British Standards Institution, London.

Byrne, B.W., Houlsby, G.T., 2003. Foundations for offshore wind turbines. Philos. Trans. R. Soc. London, Ser. A: Math. Phys. Eng. Sci. 361 (1813), 2909–2930.

Byrne, B.W., McAdam, R.A., Burd, H.J., Houlsby, G.T., Martin, C.M., Gavin, K., et al., 2015. Field Testing of Large Diameter Piles under Lateral Loading for Offshore Wind Applications.

Corbetta, G., Ho, A., Pineda, I., Ruby, K., 2015. Wind Energy Scenarios for 2030. *Ewea,* (July), pp. 1–8. Available at: http://www.ewea.org/fileadmin/files/library/publications/reports/EWEA-Wind-energy-scenarios-2030.pdf.

Cuéllar, P., Baeßler, M., Rücker, W., 2009. Ratcheting convective cells of sand grains around offshore piles under cyclic lateral loads. Granul. Matter 11 (6), 379.

Damgaard, M., Ibsen, L.B., Andersen, L.V., Andersen, J.K., 2013. Cross-wind modal properties of offshore wind turbines identified by full scale testing. J. Wind Eng. Ind. Aerod. 116, 94–108.

Dawson, T.H., 1983. Offshore Structural Engineering.

Desmond, C., Murphy, J., Blonk, L., Haans, W., 2016, September. Description of an 8 MW reference wind turbine. In: Journal of Physics: Conference Series, vol. 753. IOP Publishing, p. 92013, 9.

DNV, G., 2014. DNV-OS-J101–Design of Offshore Wind Turbine Structures. DNV GL, Oslo, Norway.

EAU, 1996. Recommendations of the Committee for the Waterfront Structures, Harbours and Waterways.

Esu, O.E., Wang, Y., Chryssanthopoulos, M., 2021. Local vibration mode pairs for damage identification in axisymmetric tubular structures. J. Sound Vib. 494, 115845 https://doi.org/10.1016/j.jsv.2020.115845. In this issue.

Ewins, D.J., 2009. Modal Testing: Theory, Practice and Application. John Wiley & Sons.

Guo, Z., Yu, L., Wang, L., Bhattacharya, S., Nikitas, G., Xing, Y., 2015. Model tests on the long-term dynamic performance of offshore wind turbines founded on monopiles in sand. J. Offshore Mech. Arctic Eng. 137 (4).

GWEC, 2020. https://gwec.net/market-to-watch-chinas-offshore-wind-industry-post-2021/.

Hu, W.H., Thöns, S., Said, S., Rücker, W., 2014. Resonance phenomenon in a wind turbine system under operational conditions. Struct. Health Monit. 12, 14.

Jalbi, S., Arany, L., Salem, A., Cui, L., Bhattacharya, S., 2019. A method to predict the cyclic loading profiles (one-way or two-way) for monopile supported offshore wind turbines. Mar. Struct. 63, 65–83.

Jonkman, J., Butterfield, S., Musial, W., Scott, G., 2009. *Definition of a 5-MW Reference Wind Turbine for Offshore System Development* (No. NREL/TP-500-38060). National Renewable Energy Lab.(NREL), Golden, CO (United States).

Kallehave, D., Thilsted, C.L., Troya, A., 2015. Observed variations of monopile foundation stiffness. In: Frontiers in Offshore Geotechnics III: Proceedings of the 3rd International Symposium on Frontiers in Offshore Geotechnics (ISFOG 2015), vol. 1. Taylor & Francis Books Ltd, pp. 717–722.

Kuhn, M., 2000. Dynamics of offshore wind energy converters on mono-pile foundation experience from the Lely offshore wind turbine. In: OWEN Workshop.

LeBlanc, C., Houlsby, G.T., Byrne, B.W., 2010. Response of stiff piles in sand to long-term cyclic lateral loading. Geotechnique 60 (2), 79–90.

Liang, R., Yuan, Y., Fu, D., Liu, R., 2020. Cyclic response of monopile-supported offshore wind turbines under wind and wave loading in sand. Mar. Georesour. Geotechnol. 1–14.

Lombardi, D., Bhattacharya, S., Wood, D.M., 2013. Dynamic soil–structure interaction of monopile supported wind turbines in cohesive soil. Soil Dynam. Earthq. Eng. 49, 165–180.

McConnell, K., Allsop, W., Allsop, N.W.H., Cruickshank, I., 2004. Piers, Jetties and Related Structures Exposed to Waves: Guidelines for Hydraulic Loadings. Thomas Telford.

Morison, J.R., Johnson, J.W., Schaaf, S.A., 1950. The force exerted by surface waves on piles. J. Petrol. Technol. 2 (5), 149–154.

Nikitas, G., Vimalan, N.J., Bhattacharya, S., 2016. An innovative cyclic loading device to study long term performance of offshore wind turbines. Soil Dynam. Earthq. Eng. 82, 154–160.

Norén-Cosgriff, K., Kaynia, A.M., 2021. Estimation of natural frequencies and damping using dynamic field data from an offshore wind turbine. Mar. Struct. 76, 102915.

Oh, K.Y., Nam, W., Ryu, M.S., Kim, J.Y., Epureanu, B.I., 2018. A review of foundations of offshore wind energy convertors: current status and future perspectives. Renew. Sustain. Energy Rev. 88, 16–36.

Shirzadeh, R., Weijtjens, W., Guillaume, P., Devriendt, C., 2015. The dynamics of an offshore wind turbine in parked conditions: a comparison between simulations and measurements. Wind Energy 18 (10), 1685–1702.

US Army Corps of Engineers, 2002. Coastal Engineering Manual. Engineer Manual 1110-2-1100. US Army Corps of Engineers, Washington, DC (in 6 volumes). http://bigfoot. wes.army.mil/cemOOl .html.

Velarde, J., Bachynski, E.E., 2017. Design and fatigue analysis of monopile foundations to support the DTU 10 MW offshore wind turbine. Energy Proc. 137, 3–13.

Versteijlen, W.G., Metrikine, A., Hoving, J.S., Smidt, E.H., De Vries, W.E., 2011. Estimation of the vibration decrement of an offshore wind turbine support structure caused by its interaction with soil. In: Proceedings of the EWEA Offshore 2011

Conference. European Wind Energy Association, Amsterdam, The Netherlands, 29 November-1 December 2011.

Vlašić, T., Seršić, D., 2021. January). Sub-Nyquist sampling in shift-invariant spaces. In: 2020 28th European Signal Processing Conference (EUSIPCO). IEEE, pp. 2284–2288.

Wang, L., Yu, L., Guo, Z., Wang, Z., 2014. Seepage induced soil failure and its mitigation during suction caisson installation in silt. J. Offshore Mech. Arctic Eng. 136 (1).

Welch, P.D., 1967. The use of Fast Fourier Transform for the estimation of power spectra: a method based on time averaging over short, modified periodograms. IEEE Trans. Audio Electroacoust. 15 (2), 70–73.

Wiser, R., Jenni, K., Seel, J., Baker, E., Hand, M., Lantz, E., Smith, A., 2016. Expert elicitation survey on future wind energy costs. Nat. Energy 1 (10), 1–8.

Xu, Y., Nikitas, G., Zhang, T., Han, Q., Chryssanthopoulos, M., Bhattacharya, S., Wang, Y., 2020. Support condition monitoring of offshore wind turbines using model updating techniques. Struct. Health Monit. 19 (4), 1017–1031.

Yeter, B., Garbatov, Y., Guedes Soares, C., 2014. Spectral fatigue assessment of an offshore wind turbine structure under wave and wind loading. In: Developments in Maritime Transportation and Exploitation of Sea Resources. Taylor & Francis Group, London, UK, pp. 425–433.

Zaaijer, M.B., 2006. Foundation modelling to assess dynamic behaviour of offshore wind turbines. Appl. Ocean Res. 28 (1), 45–57.

Zhang, J., Kang, W.H., Sun, K., Liu, F., 2019. Reliability-based serviceability limit state design of a jacket substructure for an offshore wind turbine. Energies 12 (14), 2751.

Zuo, H., Bi, K., Hao, H., et al., 2018. Dynamic analyses of operating offshore wind turbines including soilstructure interaction. Eng. Struct. 157, 42–62. https://doi. org/10.1016/j.engstruct.2017.12.001. In this issue.